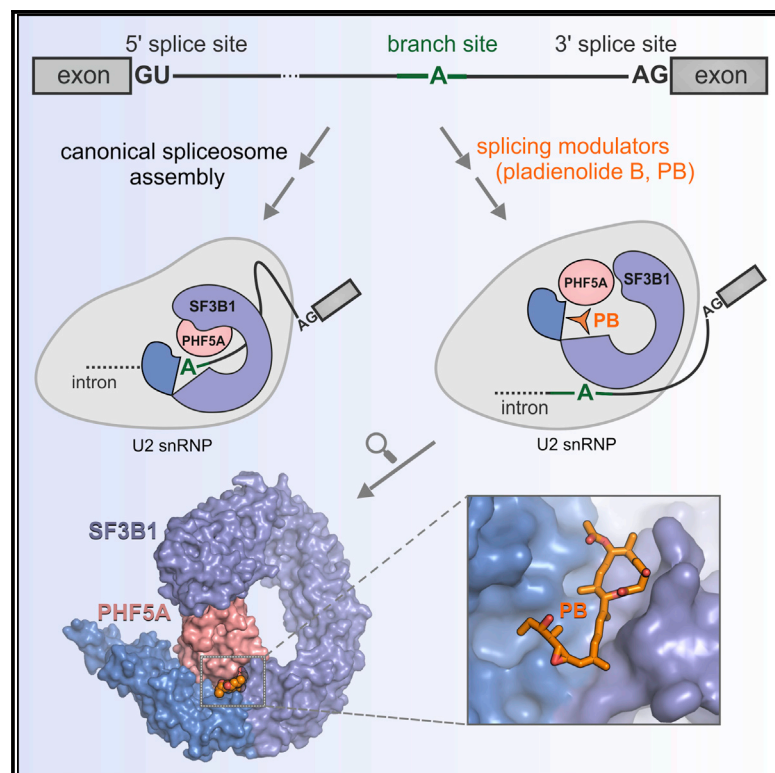


Structural Basis of Splicing Modulation by Antitumor Macrolide Compounds

Graphical Abstract



Authors

Constantin Cretu, Anant A. Agrawal, Andrew Cook, ..., Nicholas Larsen, Silvia Buonamici, Vladimir Pena

Correspondence

vladimir.pena@mpibpc.mpg.de

In Brief

Cretu et al. report the crystal structure of the multi-protein complex SF3B in complex with pladienolide B, a potent antitumor splicing modulator. The structure explains in molecular terms how the small-molecule compound and, by extension, the related splicing modulators interfere with the proper recognition of the branch site region of the intron.

Highlights

- Splicing modulators bind a hinge of SF3B1 and regulate its conformational transition
- Modulator binding regulates formation of the branch site adenosine-binding pocket
- The common pharmacophore of modulators is crucial for their molecular recognition
- Structure of pladienolide B in complex with SF3B provides a framework for drug design



Structural Basis of Splicing Modulation by Antitumor Macrolide Compounds

Constantin Cretu,¹ Anant A. Agrawal,² Andrew Cook,² Cindy L. Will,³ Peter Fekkes,² Peter G. Smith,² Reinhard Lührmann,³ Nicholas Larsen,² Silvia Buonamici,² and Vladimir Pena^{1,4,*}

¹Research Group Macromolecular Crystallography, Max Planck Institute for Biophysical Chemistry, Am Fassberg 11, 37077 Göttingen, Germany

²H3 Biomedicine, Inc., Cambridge, MA 03129, USA

³Department of Cellular Biochemistry, Max Planck Institute for Biophysical Chemistry, Am Fassberg 11, 37077 Göttingen, Germany

⁴Lead Contact

*Correspondence: vladimir.pena@mpibpc.mpg.de

<https://doi.org/10.1016/j.molcel.2018.03.011>

SUMMARY

SF3B is a multi-protein complex essential for branch site (BS) recognition and selection during pre-mRNA splicing. Several splicing modulators with antitumor activity bind SF3B and thereby modulate splicing. Here we report the crystal structure of a human SF3B core in complex with pladienolide B (PB), a macrocyclic splicing modulator and potent inhibitor of tumor cell proliferation. PB stalls SF3B in an open conformation by acting like a wedge within a hinge, modulating SF3B's transition to the closed conformation needed to form the BS adenosine-binding pocket and stably accommodate the BS/U2 duplex. This work explains the structural basis for the splicing modulation activity of PB and related compounds, and reveals key interactions between SF3B and a common pharmacophore, providing a framework for future structure-based drug design.

INTRODUCTION

Pre-mRNA splicing is an essential step of gene expression required for the removal of non-coding introns and ligation of coding exons that generate a mature mRNA. Splicing of each pair of exons occurs in two consecutive chemical reactions, both of which involve reactive groups from three locations of the intron: an adenosine from the so-called branch site (BS) and nucleotides from the 5' and 3' splice sites (SS, corresponding to the exon/intron junctions at the two ends of an intron). The entire process occurs within the spliceosome, a multi-megadalton protein-RNA complex that assembles by the stepwise recruitment of five ribonucleoprotein particles (snRNPs), named U1, U2, and U4/U6.U5, plus numerous non-snRNP proteins, to the pre-mRNA (Wahl et al., 2009). During its cyclic assembly, activation, and splicing catalysis pathway, which is driven by ATP, the spliceosome passes through several landmark stages, referred to as the E, A, B, B^{act}, B^{*}, C, C^{*}, P, and intron-lariat spliceosomal complexes (Fica and Nagai, 2017; Shi, 2017; Wahl et al., 2009).

U2 snRNP plays an important role in the recognition of the BS during constitutive and alternative splicing (Lee and Rio, 2015; Will and Lührmann, 2011). It is composed of U2 snRNA, the multimeric splicing factors SF3A and SF3B, and several other associated proteins (Will et al., 2002). In higher eukaryotes, SF3B is a hetero-heptameric complex containing SF3B1/SF3B155, SF3B2/SF3B145, SF3B3/SF3B130, SF3B4/SF3B49, SF3B5/SF3B10, SF3B6/SF3B14a, and PHF5A/SF3B14b (Will et al., 2002). In the pre-spliceosomal A complex, U2 snRNA interacts via base pairing with the BS (Wu and Manley, 1989; Zhuang and Weiner, 1989). At the same time, the U2/BS interaction is stabilized by subunits of the SF3B complex that interact with the intron, including the SF3B1 protein that contacts intron nucleotides flanking the BS adenosine (BS-A) (Gozani et al., 1996, 1998).

Several compounds with antitumor properties, such as pladienolide B (PB) (Kotake et al., 2007), herboxidiene (GEX1A) (Hasegawa et al., 2011), and spliceostatin A (SSA) (Kaida et al., 2007), bind the SF3B complex and inhibit normal pre-mRNA BS usage, inducing changes in alternative splicing patterns (Corrionero et al., 2011; Folco et al., 2011; Teng et al., 2017). Thus, SF3B is a promising target for anti-cancer therapy (Bonnal et al., 2012; Salton and Misteli, 2016). The aforementioned compounds, which are splicing inhibitors/modulators, are derived from bacterial sources (*Pseudomonas* sp and *Streptomyces* sp) and have served as templates for the synthesis of various analogs, some of which have been used in clinical trials (Bonnal et al., 2012; Lagisetti et al., 2013; Webb et al., 2013). Although their chemistry is rather diverse, all modulators from these families contain a central pharmacophore represented by a conjugated diene, flanked by two variable moieties (Bonnal et al., 2012; Effenberger et al., 2017; Lagisetti et al., 2014). However, the significance of this common organization is presently not clear.

Splicing modulators that bind SF3B (Hasegawa et al., 2011; Kaida et al., 2007; Kotake et al., 2007) arrest spliceosome assembly prior to the ATP-dependent formation of a stable A complex, leading to an "A-like" complex where U2 snRNP is less stably bound and the base pairing interactions between U2 and the intron are altered (Corrionero et al., 2011; Effenberger et al., 2014; Roybal and Jurica, 2010). By modulating BS recognition and selection in cells, these compounds lead to intron retention and exon skipping (Corrionero et al., 2011; Teng



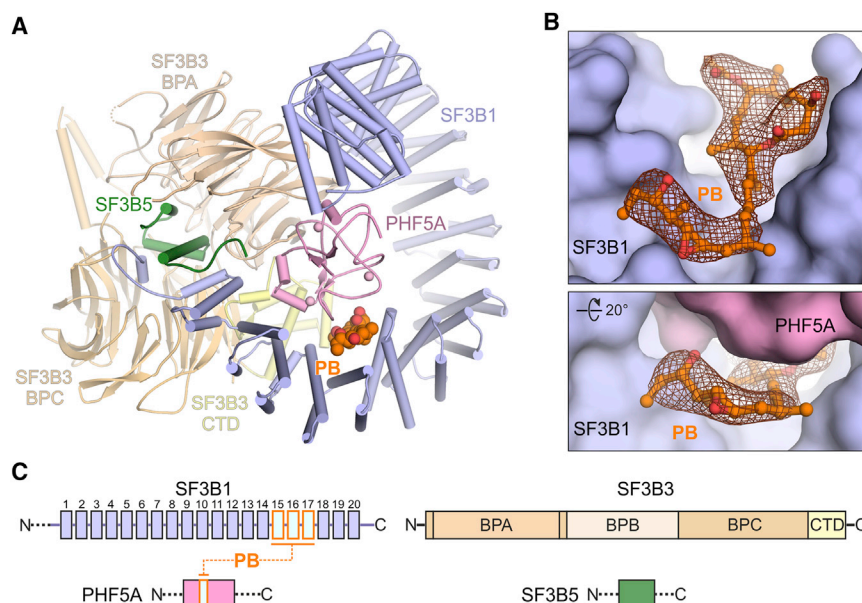


Figure 1. Overall Structure of the Human SF3B Core in Complex with PB

(A) Side view of the SF3B-PB complex. SF3B subunits are shown in different colors. The PB ligand is shown as spheres and the carbon atoms are depicted in orange.

(B) Structure of PB in the SF3B1-PHF5A pocket. PB is shown as orange sticks. The $2mF_o-DF_c$ map (brown mesh) is contoured at 1.0σ and is displayed around PB. The SF3B1 (light blue) and PHF5A (pink) subunits are shown as a surface representation.

(C) Domain composition of the SF3B core. SF3B regions forming the SF3B1-PHF5A tunnel are colored cyan and boxed in orange. Related to Figure S1.

et al., 2017; Vigeveni et al., 2017). The resulting changes in a subset of alternative splicing patterns provide an explanation for the pronounced/preferential cytotoxic activity of these compounds toward malignant versus normal cells (Lee et al., 2016; Obeng et al., 2016; Shirai et al., 2017). Cryoelectron microscopy (cryo-EM) structures of spliceosomes that are formed after the A complex, including the spliceosomal B and B^{act} complexes (Bertram et al., 2017; Plaschka et al., 2017; Rauhut et al., 2016), revealed a “closed” conformation of SF3B relative to its more “open” conformation in the isolated SF3B complex (Cretu et al., 2016). In the “closed” conformation, the terminal HEAT repeats of SF3B1 embrace the BS/U2 helix, while the reactive BS-A is shielded from the 5′ splice site in a conserved SF3B1-PHF5A pocket (Plaschka et al., 2017; Rauhut et al., 2016; Yan et al., 2016). Recent biochemical and chemogenomic analyses suggest that PB, SSA, and herboxidiene share a common binding site on SF3B, in the proximity of the BS-A-binding pocket (Effenberger et al., 2016; Teng et al., 2017). However, the precise nature of the binding site of these splicing modulators and the mechanistic consequences of their binding remain unclear.

Here we have determined the crystal structure of SF3B in complex with PB, providing a paradigm for key principles that govern molecular recognition of SF3B modulators. Together with biochemical analyses, our work reveals the mechanism whereby these compounds affect the function of SF3B and thus modulate pre-mRNA splicing.

RESULTS AND DISCUSSION

Pladienolide B Is Accommodated within an Hourglass-Shaped Tunnel that Matches the Tripartite Organization of Various SF3B Modulators

We have engineered a human SF3B core complex, comprising the HEAT domain of SF3B1/SF3B155, SF3B3/SF3B130, SF3B5/SF3B10, and PHF5A/SF3B14b, that binds a tritiated PB

derivative ($[^3\text{H}]$ -PB) in solution (Figures 1, S1A, and S1B). The complex forms crystals in the presence of PB under similar crystallization conditions as used for the previously reported apo form of the SF3B core (Cretu et al., 2016). The structure of the SF3B core complexed with PB was determined at 3.1 Å by molecular replacement using the apo form as a search model (Figures 1 and S1C–S1E; Table 1), and validated using selenium marker sites (Table 1; Figures S1F and S1G). One molecule is present in the asymmetric unit and, except for a few local changes (Figures S2A and S2B), the SF3B core complex binds PB without significant rearrangement (Figures S2C–S2F). In the crystal structure, PB is accommodated within an ~ 15 Å-long hourglass-shaped tunnel defined by seven residues from the HEAT repeats H15–H17 of SF3B1, and two residues from the trefoil-folded protein PHF5A (Figures 2A and 2B). Each “funnel” of the hourglass accommodates one of the two large moieties of PB—the macrolide head (12-membered macrocyclic group) and the aliphatic chain—while the conjugated diene that connects the two moieties is located in the constricted neck region. Importantly, the size of the tunnel suffices to accommodate all types of known SF3B modulators, and its distinctive shape can explain the common organization of the compounds in two moieties separated by a diene (Figure S3A).

The Common Pharmacophore Represented by the Conjugated Diene Is Essential for Molecular Recognition

The diene group is a key pharmacophore feature of the pladienolide, spliceostatin, and herboxidiene families of splicing modulators (Lagiseti et al., 2008, 2014) (Figure S3A). Alteration of this group (C12–C15) or changes in its immediate vicinity lead to significant decreases in activity (Bonnal et al., 2012; Effenberger et al., 2014; Lagiseti et al., 2014). Within the neck of the SF3B1-PHF5A tunnel, the five coplanar carbon atoms of the conjugated diene (C12–C15) are within interacting distances from PHF5A–Y36 and SF3B1–R1074 (Figures 2B and 2C). The diene plane is nearly perpendicular to the aromatic ring of PHF5A–Y36, indicative of π - π interactions established between these two moieties. The required molecular geometry appears to be favored by the steric

Table 1. Data Collection and Refinement Statistics

	SF3B ^{core} -PB (PDB: 6EN4)	SF3B ^{core} SeMet
Data Collection		
Space group	<i>P</i> 2 ₁ 2 ₁ 2 ₁	<i>P</i> 2 ₁ 2 ₁ 2 ₁
Wavelength (Å)	1.0	0.979
Cell dimensions: <i>a</i> , <i>b</i> , <i>c</i> (Å)	106.07, 154.57, 210.21	105.59, 153.82, 209.30
Cell dimensions: α , β , γ (°)	90.0, 90.0, 90.0	90.0, 90.0, 90.0
Resolution (Å)	48.79–3.08 (3.16–3.08) ^a	49.80–3.25 (3.34–3.25) ^a
<i>R</i> _{meas} (%)	15.7 (>100)	28.1 (>100)
<i>I</i> / σ <i>I</i>	15.4 (1.0)	10.1 (0.9)
<i>CC</i> _{1/2} (%)	99.9 (46.2)	99.7 (44.6)
Completeness (%)	100 (99.8)	99.9 (99.7)
Redundancy	13.4 (13.8)	13.3 (13.1)
Refinement		
Resolution (Å)	48.79–3.08	–
No. reflections	64,404	–
<i>R</i> _{work} / <i>R</i> _{free}	0.23/0.26	–
No. atoms: protein	17,205	–
No. atoms: ligand/ion	41	–
No. atoms: water	0	–
B factors (Å ²): protein	105.59	–
B factors (Å ²): ligand/ion	95.86	–
B factors (Å ²): water	–	–
RMSD: bond lengths (Å)	0.004	–
RMSD: bond angles (°)	0.97	–

Related to STAR Methods. RMSD, root-mean-square deviation.

^aStatistics for the highest resolution shell are shown in parentheses

constraints exerted by R1074, which flanks the diene plane on one side (Figure 2C). This distinctive ternary arrangement, where two moieties interact in a directional manner, while a third one assists in providing the required geometry, might explain why substitution of Y36 (PHF5A) has largely the same impact on PB binding as substitution of R1074 (SF3B1), as we show by scintillation proximity assays with [³H]-PB (Figures 3A and S3B). Consistent with this, we also observed in viability assays that the HCT116 cancer cell lines carrying mutations in any of these residues (PHF5A-Y36C and SF3B1-R1074H) are resistant to treatment with PB (Figure 3B) and other SF3B modulators (Teng et al., 2017). Overall, the structure shows that the invariant conjugated diene acts as a chemical rigid spacer that constrains the larger PB moieties to the hourglass-shaped tunnel, and is also an important element for molecular recognition by SF3B (Figure 2D), due to its specific interactions in the distinctive microenvironment of the neck region.

The Macrolide Ring and Aliphatic Arm Are Recognized by Shape Complementarity and a Network of Hydrophobic and Weak Polar Contacts

The 12-atom macrolide ring is largely complementary to the shape of the funnel that faces the SF3B3 subunit, where five residues provide an even distribution of contacts along its circum-

ference (Figures 2A and 2D). Thus, several contacts are established with hydrophobic regions of SF3B1 residues F1153, K1071, and V1078, which is consistent with the detrimental effects of chemical modifications of the C3 and C6 groups, with which they interact, on the activity of PB (Effenberger et al., 2014, 2017). The C7 oxycarbonyl group of the macrolide head, regarded as an important constituent of PB's pharmacophore (Lagiseti et al., 2008), is simultaneously engaged in a hydrogen bond with the backbone amide of PHF5A-R38, and a non-polar interaction with SF3B1-Y1157 (Figures 2A and 2D). Epimerization of the C7 group leads to a strong reduction in PB activity (Müller et al., 2011), and removal of the C7 oxycarbonyl group, which yields PB-OH, results in a loss of SF3B affinity and potency in cells (Figures 3B–3D). Of note is that the relatively large size of the macrolide head and the presence of the narrow neck are indicative of the likely directionality of how PB accesses the tunnel.

The aliphatic arm of PB (C16–C23) is oriented at an ~70° angle relative to the diene plane, similar to the structure of its analog herboxidiene (GEX1A) in isolation (Edmunds et al., 2000) (Figures 4A and 4B). Although this conformation is favorable for matching the shape of the tunnel, an additional ~40° rotation about the C16–C17 bond is induced in PB by the contacts with the SF3B1 residues V1110, V1114, and F1153, and PHF5A-Y36 (Figures 2A, 4C, and 4D). The latter two residues simultaneously contact both the aliphatic arm and the other PB moieties, likely leading to additional restrictions in the conformational freedom, which enhances stable binding of the compound to SF3B. These “bridging” interactions can explain why chemical modifications at distant positions of PB reduce its activity only when they occur simultaneously (Effenberger et al., 2014, 2017). Thus, removal of the methyl groups from C16 and C20 or modification of the epoxy group (C18–C19) and of the C11–C12 bond decreases PB activity substantially (Effenberger et al., 2014, 2017).

PB Blocks a Conformational Change in SF3B, Preventing Formation of the BS-A Pocket and Accommodation of the BS/U2 Duplex

In the crystal structure of isolated complexes, SF3B has been observed in an “open” conformation, whose functional importance was unclear as it could not be clearly assigned to a precise step of the splicing cycle (Cretu et al., 2016). In the “open” conformation, the distance between the terminal HEAT repeats is too large to stably accommodate the U2/BS helix (Cretu et al., 2016). In contrast, SF3B1 adopts a “closed” conformation in fully assembled spliceosomes, where it “clamps down” on the U2/BS helix and likely stabilizes the U2/BS interaction (Bertram et al., 2017; Plaschka et al., 2017; Yan et al., 2016). The “closed” SF3B1 conformation is likely to arise within A complexes where U2 snRNA pairs with the BS and SF3B1 contacts nucleotides flanking the BS-A (Gozani et al., 1996, 1998). Importantly, in the presence of PB, SF3B1 exhibits the “open” conformation that is likely to be also present in the “A-like” complexes stalled by SF3B modulators (Corrionero et al., 2011; Folco et al., 2011; Roybal and Jurica, 2010). Structural comparison between the “open” and “closed” conformations of SF3B1 (Rauhut et al., 2016; Yan et al., 2016) revealed that the two structures differ substantially with respect to the position of HEAT repeats H1–H15

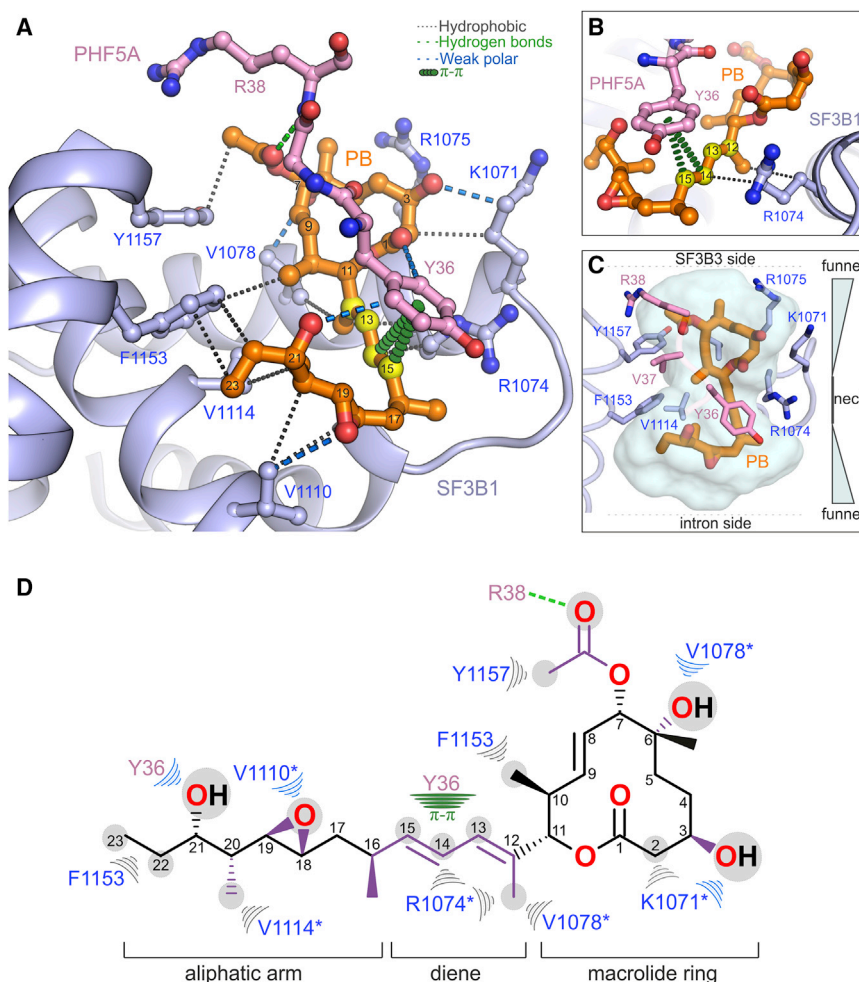


Figure 2. PB Binding to the SF3B1-PHF5A Tunnel

(A) PB is engaged in multiple contacts with residues that define the tunnel. PB (orange) is shown in stick representation and the carbon atoms of the conjugated diene moiety are shown in yellow. SF3B side chains within ~ 4 Å of PB are shown as sticks. V37 side chain was omitted for clarity.

(B) Overview of the PB-binding tunnel. The interface between SF3B1 H15-H17 HEAT repeats (light blue) and PHF5A (pink) is shown as a surface model and the superimposed PB ligand is represented as orange sticks.

(C) The interactions of the Y36 (PHF5A) and R1074 (SF3B1) residues with the diene moiety of PB. The π - π interactions are colored dark green and are shown as stacked disks, while hydrophobic interactions are depicted as gray dotted lines.

(D) Schematic of the PB interaction with SF3B1 (light blue) and PHF5A (pink). SF3B residues within ~ 4 Å of PB are shown. Chemical groups that are important for the activity of PB are colored purple. Hydrogen bonds are depicted as dotted green lines; hydrophobic and weak polar contacts are shown as gray and blue semicircles, respectively. The π - π interactions are colored dark green. In the closed SF3B conformation found in the spliceosome, PB's binding site is reconfigured, such that those residues marked with an asterisk are displaced from the unmarked ones.

Related to Figure S2.

BS-A pocket (Figures 5, S4F, and S4G). By occupying the tunnel, the modulator stabilizes SF3B1 in the “open” conformation, acting as a “wedge” that prevents rotation of the SF3B1 hinge. Consequently, the induced fit transition to the

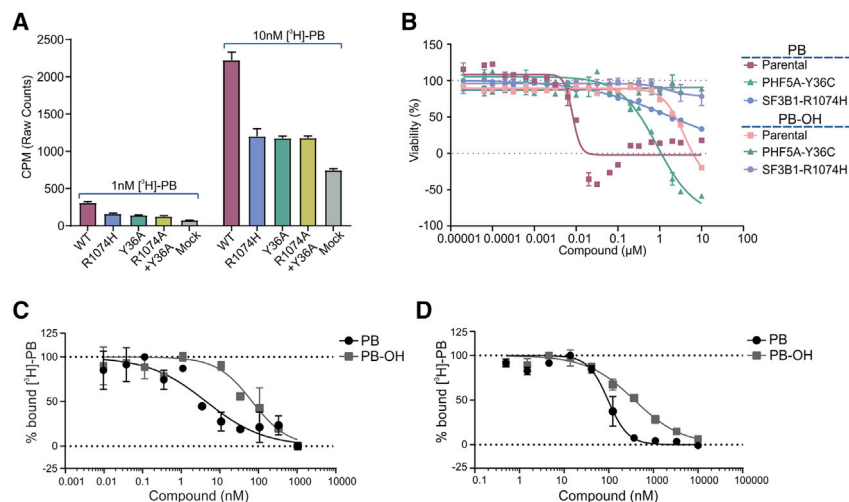
relative to the rest of the SF3B core (including H16-H20 and the other three proteins) (Figures S4A–S4E). This large conformational difference is due to the pivoting ($\sim 23^\circ$ rotation) of H1-H15 via a hinge located in the H15-H17 region of SF3B1 (Figures 5A and S4A–S4E). Intriguingly, the binding sites of both PB and the BS-A are present within the same SF3B1 hinge region, in the “open” and “closed” conformation, respectively (Figures 5A and 5B). In spite of their partial overlap, the sites are significantly different in the two states of SF3B1. Thus, SF3B1 residues that form the binding site of PB in the “open” conformation are repositioned in the “closed” state (Figures 2D, 5C, and 5D), where several of them become part of the BS-A pocket (i.e., V1114, K1071, V1078, and R1074; Figures S4F and S4G). At the same time, PHF5A-Y36 is also reoriented in the “closed” conformation to form a hydrogen bond with SF3B1-K1071, which in turn contacts the 3'-hydroxyl moiety of the reactive adenosine (Figures S4F and S4G).

Overall, the structural comparison indicates that a transition of SF3B1 from the “open” to the “closed” state, likely occurring during the assembly of the A complex, would entail the pivoting of HEAT repeats H1-H15 via the hinge region, with concomitant deconstruction of the PB-binding tunnel and formation of the

“closed” conformation is impaired, inhibiting formation of the BS-A pocket and stable accommodation of the BS/U2 duplex, and possibly even its formation (Corrionero et al., 2011; Folco et al., 2011) (Figure 5E). Conversely, once the “closed” conformation is achieved, SF3B should no longer be able to bind PB. Indeed, purified B complexes, which have been shown to contain SF3B with a “closed” conformation (Bertram et al., 2017; Plaschka et al., 2017), can be chased into catalytically active spliceosomes even in the presence of PB (Figure S5), consistent with the idea that PB can no longer bind SF3B.

Variations in the Affinity of Modulators for SF3B Lead to Differential Splicing Inhibition with Different Pre-mRNA Substrates

The ability of PB, as well as of other splicing modulators, to block the conformational change in SF3B1 during A complex formation explains the inhibitory effect of these compounds on pre-mRNA splicing observed *in vitro* (Corrionero et al., 2011; Effenberger et al., 2016; Folco et al., 2011). However, introns exhibit differential sensitivity to SF3B modulators in cells, resulting in intron retention and/or exon skipping rather than a general arrest of splicing (Corrionero et al., 2011; Teng et al., 2017). We thus



monoaffinity from HeLa nuclear extract. PB-OH derivative, which lacks the C7 oxycarbonyl group, displays a reduced affinity toward SF3B compared to PB ($IC_{50} = 78$ nM versus $IC_{50} = 5$ nM for PB). Error bar indicates SD, $n = 3$.

(D) Competitive titration of [³H]-PB (1 nM) with PB (orange) or PB-OH (magenta) by SPA using the recombinant full-length SF3B complex (12.5 nM). The PB-OH derivative lacks the C7 oxycarbonyl group and, as a result, exhibits reduced affinity for SF3B ($IC_{50} = 378$ nM versus $IC_{50} = 97$ nM for PB). Error bar indicates SD, $n = 3$.

Related to Figure S3.

next investigated whether there is a correlation between the affinity of a modulator for wild-type SF3B and its ability to inhibit the splicing *in vitro* of different pre-mRNAs. To this end, we tested splicing of substrates that differ with respect to the “strength” of the BS and/or poly-pyrimidine tract (PPT, i.e., the extent to which the BS and PPT differ from the consensus sequences). To produce the “weakest” BS variant, we incorporated an adjacent “decoy” sequence (Corrionero et al., 2011), meant to provide an alternative, unproductive site for binding

of U2 snRNA. Notably, PB inhibits splicing efficiently, regardless of the “strength” of the BS or PPT, or the presence of a “decoy” sequence (Figures 6A and S6A). However, a PB derivative with reduced affinity for SF3B, such as PB-OH, is still able to inhibit splicing of pre-mRNA with a “weak” BS, but it is much less effective when a “strong” BS is present (Figures 6B and S6A). In contrast, there was no difference observed with the wild-type versus “weak” PPT (Figures 6B and S6A). This suggests that the correlation between affinity and the “strength” of the

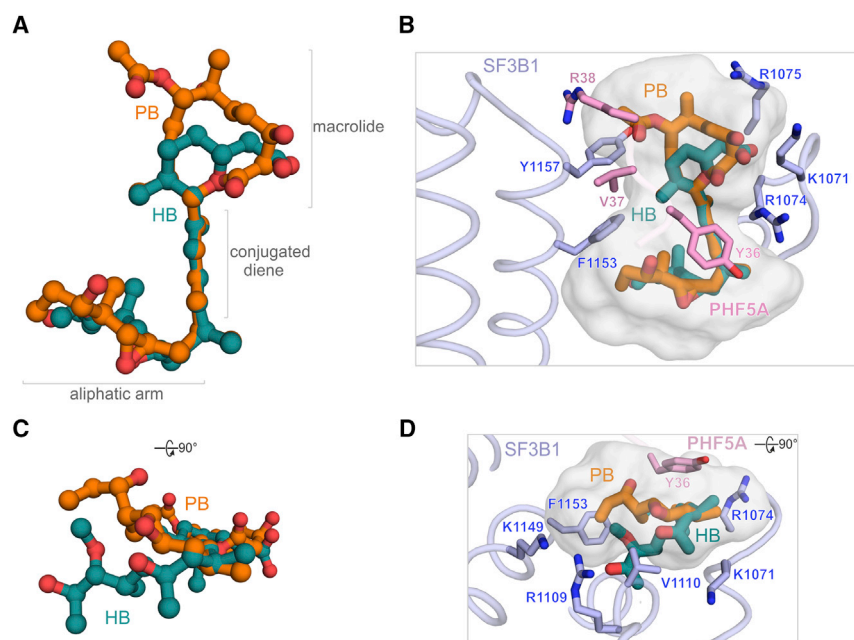


Figure 4. Comparison of PB and HB Structural Features

(A and C) Structural superposition of PB (orange) with the small molecule crystal structure of herboxidiene (HB, teal). The superposition was carried out using the common C12-C16 moiety as a reference. The aliphatic arm adopts different positions in the two structures, while the functionalized pyran ring of HB superimposes onto the PB 12-membered macrocycle. In (C), the structure is depicted as in (A) and rotated as indicated.

(B and D) Tentative location of HB in the SF3B1-PHF5A tunnel. The pyran ring of HB (teal) likely occupies the top SF3B “funnel,” as observed with the PB macrocycle. The aliphatic arm of HB is likely located in the bottom “funnel” and may rearrange upon binding to SF3B1-PHF5A. SF3B1 (light blue) and PHF5A (pink) are displayed and colored as in Figure 2A. In (D), the structure is depicted as in (B) and rotated as indicated.

Related to Figure S3.

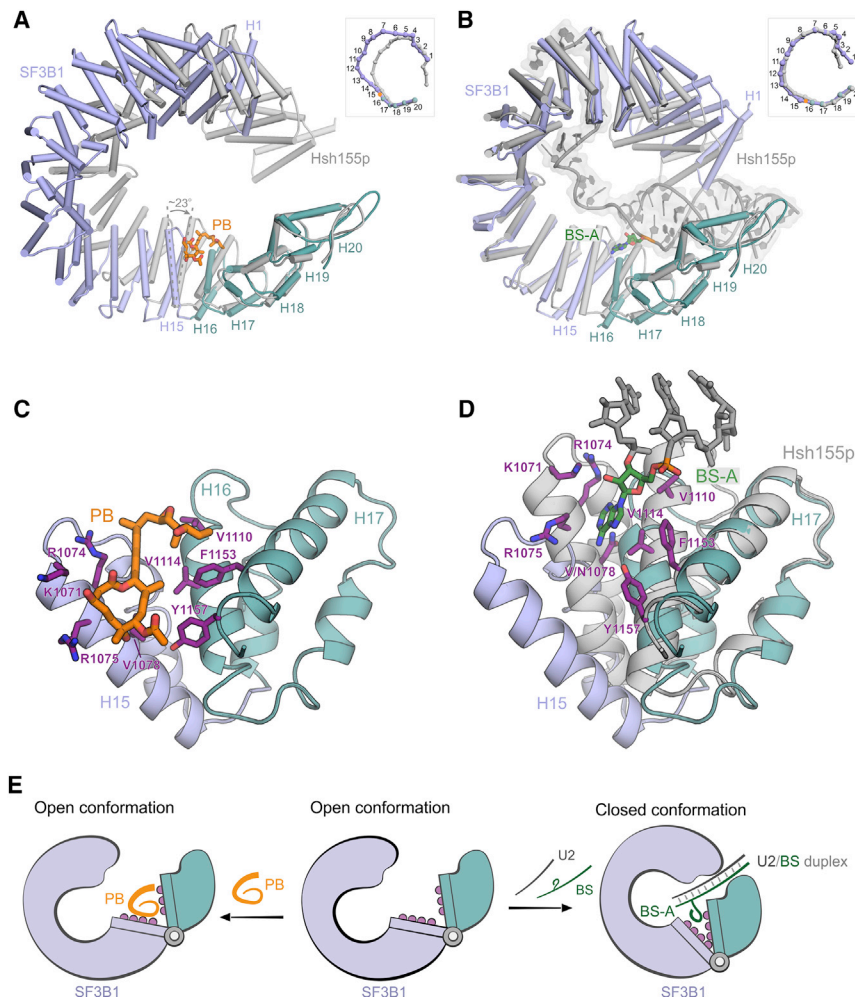


Figure 5. PB and the BS-A Bind SF3B1 in the Same Hinge Region in the Open and Closed Conformation

(A) The SF3B1 HEAT domain ("open" conformation) in complex with PB (orange sticks) and that of *S. cerevisiae* Hsh155p ("closed" conformation, gray) are aligned via the equivalent H16-H20 region (cyan). H1-H15 repeats are shown in light blue. The inset depicts a schematic of the superposition with the centroids of each HEAT repeat shown as spheres.

(B) Structural superposition of H1-H15 and H16-H20 regions of SF3B1 (as separate rigid bodies) with the equivalent regions of Hsh155p. The U2/BS helix and the downstream region of the intron, as seen in the yeast activated spliceosome, are shown in gray. The bulged BS adenosine (BS-A) is highlighted in deep green.

(C) The H15-H17 hinge region of SF3B1 (light blue) in the presence of PB.

(D) The H15-H17 hinges of SF3B1 and Hsh155p (gray) superimposed as in Figure 4A. PB is omitted for clarity and the BS-A is shown. Several residues of PB's binding pocket, as well as the equivalent residues from Hsh155p in the "closed" conformation, are shown in the left and right figures, respectively.

(E) Schematic overview of the mechanism of action of PB. The "open" conformation of SF3B1 is likely found in the U2 snRNP, prior to the stable formation of the A complex. The splicing modulator PB (orange) binds SF3B1 in the "open" state, preventing the stable accommodation of the U2/BS helix and the BS-A, which requires a "closed" conformation of the protein. The hinge (two rectangular elements connected by a ring) and the HEAT repeats H16-H20 (teal) and H1-H15 (light blue) are indicated.

Related to Figures S4 and S5.

substrate's BS enables these compounds to act as modulators rather than mere blockers of splicing (Figure S6B), consistent with their ability to selectively modulate splicing patterns in cells (Corrionero et al., 2011; Teng et al., 2017). Importantly, the model that we derived from our structural data indicates that a direct competition between the BS-A and the modulator is unlikely (Figure 5E) because the binding sites of the two ligands do not exist

simultaneously (i.e., one is present in the "open" and the other in the "closed" conformation). Therefore, our model supports the idea that the intron and the modulator compete for the same conformation ("open" form) of SF3B1, rather than for the same binding site. That is, "strong" substrates exhibit higher base pair complementarity within the U2/BS duplex, favoring a shift of the equilibrium from the "open" toward the "closed" state,

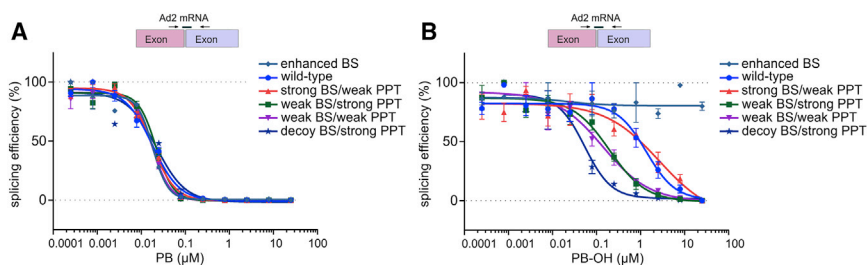


Figure 6. Differential Splicing Inhibition of Various Pre-mRNA Substrates Is Dependent on the Affinity of the Modulator for SF3B1

In vitro splicing assays of substrates derived from the Ad2 model pre-mRNA, in the presence of PB (A) or PB-OH (B). Formation of spliced products was monitored by qRT-PCR and the splicing efficiency (%) was determined relative to the DMSO-treated samples. PB exerts its inhibitory action in a 3' SS sequence-independent manner, whereas the less potent compound, PB-OH, exhibits an apparent sequence-dependent inhibition profile. Related to Figure S6.

likely via an induced fit mechanism, if the modulator binds with sufficiently weak affinity and therefore cannot act as an effective “wedge” (Figure S6B). Conversely, potent antagonists (such as PB), with high affinity for the “open” state of SF3B1, would shift the equilibrium toward a tightly bound “open” state and therefore compete efficiently with a wider range of pre-mRNAs. Similar differential effects were recently observed for the more potent modulator spliceostatin A versus sudemycins (Vigevani et al., 2017).

In light of this model, the correlation between the affinity of modulators for the SF3B-binding tunnel and their ability to selectively alter splicing of various pre-mRNA substrates suggests future strategies for manipulating/tuning their splicing modulation properties by structure-guided modification of their binding affinity.

Concluding Remarks

The crystal structure of the SF3B core in complex with PB advances a unified view on the structural definition of SF3B modulators, and on the structural basis for their inhibitory and modulatory effects on splicing. The hourglass-shaped SF3B tunnel and the contacts with PB explain the tripartite organization of SF3B modulators into two chemically variable moieties connected by an invariant diene—the key components for molecular recognition. From a mechanistic perspective, the structural and biochemical analyses reveal the significance of an early open SF3B conformation and of its conversion to the closed conformation, and indicate how modulators exploit the presence of a functional hinge to inhibit BS usage and modulate splicing.

STAR★METHODS

Detailed methods are provided in the online version of this paper and include the following:

- KEY RESOURCES TABLE
- CONTACT FOR REAGENT AND RESOURCE SHARING
- EXPERIMENTAL MODEL AND SUBJECT DETAILS
 - Cell lines
- METHOD DETAILS
 - Expression and purification of recombinant SF3B complexes
 - Crystallization and structure determination of the human SF3B core in complex with PB
 - Structural superposition of SF3B1 and Hsh155p
 - Cell viability assays
 - HeLa nuclear extract preparation
 - In vitro splicing assays
 - Scintillation proximity assays/competitive binding assay
 - Affinity purification of B complexes and splicing chase experiments
- QUANTIFICATION AND STATISTICAL ANALYSIS
- DATA AND SOFTWARE AVAILABILITY

SUPPLEMENTAL INFORMATION

Supplemental Information includes six figures and can be found with this article online at <https://doi.org/10.1016/j.molcel.2018.03.011>.

ACKNOWLEDGMENTS

We thank the staff (Anuschka Pauluhn, Isabelle Martiel, Vincent Olieric, and Justyna Wojdyla) from the X10SA beamline (Swiss Light Source, PSI Villigen, Switzerland) for assistance with data collection. We are grateful to Gabi Heyne, Betty Chan, Sean Irwin, Benjamin Caleb, and Craig Karr for technical assistance. We thank H3 Biomedicine employees for their support in the presented project. This study was supported by the Max Planck Society (C.C., C.L.W., R.L., and V.P.).

AUTHOR CONTRIBUTIONS

C.C. purified, crystallized, and determined the structure of the SF3B core in complex with PB. C.C. expressed and purified SF3B mutants. C.C. and V.P. performed structural analyses. A.A.A., N.L., and P.F. performed and guided the *in vitro* biochemical assays. P.G.S., S.B., and A.C. performed and led the *in vitro* cellular assay testing. C.L.W. and R.L. performed the affinity purification of B complexes and the chase experiment. V.P. initiated and coordinated the project. The manuscript was finalized with input from all authors. Requests for cell lines and RNA substrates should be addressed to S.B. (silvia_buonamici@h3biomedicine.com). Correspondence for the manuscript should be addressed to V.P. (vlad.pena@mpibpc.mpg.de).

DECLARATION OF INTERESTS

C.C., C.L.W., R.L., and V.P. declare no competing interests. A.A.A., A.C., P.F., N.L., P.G.S., and S.B. are employees of H3 Biomedicine, Inc.

Received: November 6, 2017

Revised: February 7, 2018

Accepted: March 7, 2018

Published: April 12, 2018

REFERENCES

- Abe, F., and Hiraki, T. (2009). Mechanistic role of ergosterol in membrane rigidity and cycloheximide resistance in *Saccharomyces cerevisiae*. *Biochim. Biophys. Acta* 1788, 743–752.
- Adams, P.D., Afonine, P.V., Bunkóczi, G., Chen, V.B., Davis, I.W., Echols, N., Headd, J.J., Hung, L.W., Kapral, G.J., Grosse-Kunstleve, R.W., et al. (2010). PHENIX: a comprehensive Python-based system for macromolecular structure solution. *Acta Crystallogr. D Biol. Crystallogr.* 66, 213–221.
- Bertram, K., Agafonov, D.E., Dybkov, O., Haselbach, D., Leelaram, M.N., Will, C.L., Urlaub, H., Kastner, B., Lührmann, R., and Stark, H. (2017). Cryo-EM structure of a pre-catalytic human spliceosome primed for activation. *Cell* 170, 701–713.e11.
- Bessonov, S., Anokhina, M., Will, C.L., Urlaub, H., and Lührmann, R. (2008). Isolation of an active step I spliceosome and composition of its RNP core. *Nature* 452, 846–850.
- Bonnal, S., Vigevani, L., and Valcárcel, J. (2012). The spliceosome as a target of novel antitumour drugs. *Nat. Rev. Drug Discov.* 11, 847–859.
- Corrionero, A., Miñana, B., and Valcárcel, J. (2011). Reduced fidelity of branch point recognition and alternative splicing induced by the anti-tumor drug spliceostatin A. *Genes Dev.* 25, 445–459.
- Cretu, C., Schmitzová, J., Ponce-Salatierra, A., Dybkov, O., De Laurentiis, E.I., Sharma, K., Will, C.L., Urlaub, H., Lührmann, R., and Pena, V. (2016). Molecular architecture of SF3b and structural consequences of its cancer-related mutations. *Mol. Cell* 64, 307–319.
- Edmunds, A.J., Arnold, G., Hagmann, L., Schaffner, R., and Furlenmeier, H. (2000). Synthesis of simplified herboxidiene aromatic hybrids. *Bioorg. Med. Chem. Lett.* 10, 1365–1368.
- Effenberger, K.A., Anderson, D.D., Bray, W.M., Prichard, B.E., Ma, N., Adams, M.S., Ghosh, A.K., and Jurica, M.S. (2014). Coherence between cellular responses and *in vitro* splicing inhibition for the anti-tumor drug pladienolide B and its analogs. *J. Biol. Chem.* 289, 1938–1947.

- Effenberg, K.A., Urabe, V.K., Prichard, B.E., Ghosh, A.K., and Jurica, M.S. (2016). Interchangeable SF3B1 inhibitors interfere with pre-mRNA splicing at multiple stages. *RNA* 22, 350–359.
- Effenberg, K.A., Urabe, V.K., and Jurica, M.S. (2017). Modulating splicing with small molecular inhibitors of the spliceosome. *Wiley Interdiscip. Rev. RNA* 8, <https://doi.org/10.1002/wrna.1381>.
- Emsley, P., and Cowtan, K. (2004). Coot: model-building tools for molecular graphics. *Acta Crystallogr. D Biol. Crystallogr.* 60, 2126–2132.
- Emsley, P., Lohkamp, B., Scott, W.G., and Cowtan, K. (2010). Features and development of Coot. *Acta Crystallogr. D Biol. Crystallogr.* 66, 486–501.
- Evans, P.R., and Murshudov, G.N. (2013). How good are my data and what is the resolution? *Acta Crystallogr. D Biol. Crystallogr.* 69, 1204–1214.
- Fica, S.M., and Nagai, K. (2017). Cryo-electron microscopy snapshots of the spliceosome: structural insights into a dynamic ribonucleoprotein machine. *Nat. Struct. Mol. Biol.* 24, 791–799.
- Fitzgerald, D.J., Berger, P., Schaffitzel, C., Yamada, K., Richmond, T.J., and Berger, I. (2006). Protein complex expression by using multigene baculoviral vectors. *Nat. Methods* 3, 1021–1032.
- Folco, E.G., Coil, K.E., and Reed, R. (2011). The anti-tumor drug E7107 reveals an essential role for SF3b in remodeling U2 snRNP to expose the branch point-binding region. *Genes Dev.* 25, 440–444.
- Gozani, O., Feld, R., and Reed, R. (1996). Evidence that sequence-independent binding of highly conserved U2 snRNP proteins upstream of the branch site is required for assembly of spliceosomal complex. *Genes Dev.* 10, 233–243.
- Gozani, O., Potashkin, J., and Reed, R. (1998). A potential role for U2AF-SAP 155 interactions in recruiting U2 snRNP to the branch site. *Mol. Cell. Biol.* 18, 4752–4760.
- Hasegawa, M., Miura, T., Kuzuya, K., Inoue, A., Won Ki, S., Horinouchi, S., Yoshida, T., Kunoh, T., Koseki, K., Mino, K., et al. (2011). Identification of SAP155 as the target of GEX1A (Herboxidiene), an antitumor natural product. *ACS Chem. Biol.* 6, 229–233.
- Jubb, H.C., Higuero, A.P., Ochoa-Montañón, B., Pitt, W.R., Ascher, D.B., and Blundell, T.L. (2017). Arpeggio: a web server for calculating and visualising interatomic interactions in protein structures. *J. Mol. Biol.* 429, 365–371.
- Kabsch, W. (2010). Xds. *Acta Crystallogr. D Biol. Crystallogr.* 66, 125–132.
- Kaida, D., Motoyoshi, H., Tashiro, E., Nojima, T., Hagiwara, M., Ishigami, K., Watanabe, H., Kitahara, T., Yoshida, T., Nakajima, H., et al. (2007). Spliceostatin A targets SF3b and inhibits both splicing and nuclear retention of pre-mRNA. *Nat. Chem. Biol.* 3, 576–583.
- Kotake, Y., Sagane, K., Owa, T., Mimori-Kiyosue, Y., Shimizu, H., Uesugi, M., Ishihama, Y., Iwata, M., and Mizui, Y. (2007). Splicing factor SF3b as a target of the antitumor natural product pladienolide. *Nat. Chem. Biol.* 3, 570–575.
- Lagiseti, C., Pourpak, A., Jiang, Q., Cui, X., Goronga, T., Morris, S.W., and Webb, T.R. (2008). Antitumor compounds based on a natural product consensus pharmacophore. *J. Med. Chem.* 51, 6220–6224.
- Lagiseti, C., Palacios, G., Goronga, T., Freeman, B., Caufield, W., and Webb, T.R. (2013). Optimization of antitumor modulators of pre-mRNA splicing. *J. Med. Chem.* 56, 10033–10044.
- Lagiseti, C., Yermolina, M.V., Sharma, L.K., Palacios, G., Prigaro, B.J., and Webb, T.R. (2014). Pre-mRNA splicing-modulatory pharmacophores: the total synthesis of herboxidiene, a pladienolide-herboxidiene hybrid analog and related derivatives. *ACS Chem. Biol.* 9, 643–648.
- Lee, Y., and Rio, D.C. (2015). Mechanisms and regulation of alternative pre-mRNA splicing. *Annu. Rev. Biochem.* 84, 291–323.
- Lee, S.C., Dvinge, H., Kim, E., Cho, H., Micol, J.B., Chung, Y.R., Durham, B.H., Yoshimi, A., Kim, Y.J., Thomas, M., et al. (2016). Modulation of splicing catalysis for therapeutic targeting of leukemia with mutations in genes encoding spliceosomal proteins. *Nat. Med.* 22, 672–678.
- Liebschner, D., Afonine, P.V., Moriarty, N.W., Poon, B.K., Sobolev, O.V., Terwilliger, T.C., and Adams, P.D. (2017). Polder maps: improving OMIT maps by excluding bulk solvent. *Acta Crystallogr. D Struct. Biol.* 73, 148–157.
- Luo, M.J., and Reed, R. (1999). Splicing is required for rapid and efficient mRNA export in metazoans. *Proc. Natl. Acad. Sci. USA* 96, 14937–14942.
- Makarov, E.M., Makarova, O.V., Urlaub, H., Gentzel, M., Will, C.L., Wilm, M., and Lührmann, R. (2002). Small nuclear ribonucleoprotein remodeling during catalytic activation of the spliceosome. *Science* 298, 2205–2208.
- McCoy, A.J. (2007). Solving structures of protein complexes by molecular replacement with Phaser. *Acta Crystallogr. D Biol. Crystallogr.* 63, 32–41.
- Müller, S., Mayer, T., Sasse, F., and Maier, M.E. (2011). Synthesis of a pladienolide B analogue with the fully functionalized core structure. *Org. Lett.* 13, 3940–3943.
- Obeng, E.A., Chappell, R.J., Seiler, M., Chen, M.C., Campagna, D.R., Schmidt, P.J., Schneider, R.K., Lord, A.M., Wang, L., Gambe, R.G., et al. (2016). Physiologic expression of SF3b1(K700E) causes impaired erythropoiesis, aberrant splicing, and sensitivity to therapeutic spliceosome modulation. *Cancer Cell* 30, 404–417.
- Pellizzoni, L., Kataoka, N., Charroux, B., and Dreyfuss, G. (1998). A novel function for SMN, the spinal muscular atrophy disease gene product, in pre-mRNA splicing. *Cell* 95, 615–624.
- Pettersen, E.F., Goddard, T.D., Huang, C.C., Couch, G.S., Greenblatt, D.M., Meng, E.C., and Ferrin, T.E. (2004). UCSF Chimera—a visualization system for exploratory research and analysis. *J. Comput. Chem.* 25, 1605–1612.
- Plaschka, C., Lin, P.C., and Nagai, K. (2017). Structure of a pre-catalytic spliceosome. *Nature* 546, 617–621.
- Rauhut, R., Fabrizio, P., Dybkov, O., Hartmuth, K., Pena, V., Chari, A., Kumar, V., Lee, C.T., Urlaub, H., Kastner, B., et al. (2016). Molecular architecture of the *Saccharomyces cerevisiae* activated spliceosome. *Science* 353, 1399–1405.
- Roybal, G.A., and Jurica, M.S. (2010). Spliceostatin A inhibits spliceosome assembly subsequent to prespliceosome formation. *Nucleic Acids Res.* 38, 6664–6672.
- Salentin, S., Schreiber, S., Haupt, V.J., Adasme, M.F., and Schroeder, M. (2015). PLIP: fully automated protein-ligand interaction profiler. *Nucleic Acids Res.* 43 (W1), W443–7.
- Salton, M., and Misteli, T. (2016). Small molecule modulators of pre-mRNA splicing in cancer therapy. *Trends Mol. Med.* 22, 28–37.
- Shi, Y. (2017). Mechanistic insights into precursor messenger RNA splicing by the spliceosome. *Nat. Rev. Mol. Cell Biol.* 18, 655–670.
- Shirai, C.L., White, B.S., Tripathi, M., Tapia, R., Ley, J.N., Ndonwi, M., Kim, S., Shao, J., Carver, A., Saez, B., et al. (2017). Mutant U2AF1-expressing cells are sensitive to pharmacological modulation of the spliceosome. *Nat. Commun.* 8, 14060.
- Teng, T., Tsai, J.H., Puyang, X., Seiler, M., Peng, S., Prajapati, S., Aird, D., Buonamici, S., Caleb, B., Chan, B., et al. (2017). Splicing modulators act at the branch point adenosine binding pocket defined by the PHF5A-SF3b complex. *Nat. Commun.* 8, 15522.
- Vigevani, L., Gohr, A., Webb, T., Irimia, M., and Valcárcel, J. (2017). Molecular basis of differential 3' splice site sensitivity to anti-tumor drugs targeting U2 snRNP. *Nat. Commun.* 8, 2100.
- Villa, R., Kashyap, M.K., Kumar, D., Kippes, T.J., Castro, J.E., La Clair, J.J., and Burkart, M.D. (2013). Stabilized cyclopropane analogs of the splicing inhibitor FD-895. *J. Med. Chem.* 56, 6576–6582.
- Wahl, M.C., Will, C.L., and Lührmann, R. (2009). The spliceosome: design principles of a dynamic RNP machine. *Cell* 136, 701–718.
- Webb, T.R., Joyner, A.S., and Potter, P.M. (2013). The development and application of small molecule modulators of SF3b as therapeutic agents for cancer. *Drug Discov. Today* 18, 43–49.
- Will, C.L., and Lührmann, R. (2011). Spliceosome structure and function. *Cold Spring Harb. Perspect. Biol.* 3, a003707.

- Will, C.L., Urlaub, H., Achsel, T., Gentzel, M., Wilm, M., and Lührmann, R. (2002). Characterization of novel SF3b and 17S U2 snRNP proteins, including a human Prp5p homologue and an SF3b DEAD-box protein. *EMBO J.* 21, 4978–4988.
- Winn, M.D., Ballard, C.C., Cowtan, K.D., Dodson, E.J., Emsley, P., Evans, P.R., Keegan, R.M., Krissinel, E.B., Leslie, A.G., McCoy, A., et al. (2011). Overview of the CCP4 suite and current developments. *Acta Crystallogr. D Biol. Crystallogr.* 67, 235–242.
- Wu, J., and Manley, J.L. (1989). Mammalian pre-mRNA branch site selection by U2 snRNP involves base pairing. *Genes Dev.* 3, 1553–1561.
- Yan, C., Wan, R., Bai, R., Huang, G., and Shi, Y. (2016). Structure of a yeast activated spliceosome at 3.5 Å resolution. *Science* 353, 904–911.
- Zhuang, Y., and Weiner, A.M. (1989). A compensatory base change in human U2 snRNA can suppress a branch site mutation. *Genes Dev.* 3, 1545–1552.

STAR★METHODS

KEY RESOURCES TABLE

REAGENT or RESOURCE	SOURCE	IDENTIFIER
Antibodies		
Anti-FLAG antibody	Sigma-Aldrich	Cat#F3165, lot #SLBQ7119V, clone M2
Anti-SF3B3 antibody	Abcam	Cat#AB209403, clone EPR18441
Anti-SF3B1 antibody	MBL	Cat#D221-3, clone 16
Bacterial and Virus Strains		
<i>Escherichia coli</i> BW23474	Dr. Imre Berger, EMBL, Grenoble	N/A
<i>Escherichia coli</i> DH10MultiBacY	Dr. Imre Berger, EMBL, Grenoble	N/A
<i>Escherichia coli</i> XL-10 Gold	Agilent Technologies	Cat#200314
<i>Escherichia coli</i> Rosetta 2 (DE3)	Merck	Cat#71397
Chemicals, Peptides, and Recombinant Proteins		
Pladienolide B (PB), used in crystallization trials	Santa Cruz Biotechnology	Cat#sc-391691
Pladienolide B (PB), used in viability assays, scintillation proximity assays, and <i>in vitro</i> splicing assays	This work, Kotake et al., 2007	N/A
[³ H]-labeled pladienolide B ([³ H]-PB), used in scintillation proximity assays	This work, Kotake et al., 2007	N/A
Pladienolide A (PB-OH), used in viability assays, scintillation proximity assays, and <i>in vitro</i> splicing assays	This work, Kotake et al., 2007	N/A
cOmplete Protease Inhibitor Cocktail	Roche	Cat#11836145001
Ampicillin	Carl Roth	Cat#K029.3
Gentamycin	Carl Roth	Cat#0233.4
Kanamycin	Carl Roth	Cat#T832.3
Spectinomycin	Sigma-Aldrich	Cat#S4014
Tetracycline	Sigma-Aldrich	Cat#T8032
IPTG	Carl Roth	Cat#2316.5
X-Gal	Sigma-Aldrich	Cat#B4252
Imidazole	Sigma-Aldrich	Cat#56750
Maltose	Sigma-Aldrich	Cat#M5885
L-Glutathione reduced	Sigma-Aldrich	Cat#G4251
Seleno-L-methionine	Sigma-Aldrich	Cat#S3132
Pentaerythritol propoxylate (5/4 PO/OH)	Sigma-Aldrich	Cat#418749
MS2-MBP	in-house	N/A
T7 RNA polymerase	in-house	N/A
<i>Pfu</i> DNA polymerase	in-house	N/A
RNasin	Promega	Cat#N2511
RQ1 RNase-Free DNase	Promega	Cat#M6101
TEV (Tobacco Etch Virus) protease	in-house	N/A
PreScission protease	GE Healthcare	Cat#27-0843-01
Cre Recombinase	New England Biolabs	Cat#M0298
Sf-900 III SFM insect cell culture medium	Thermo Fisher Scientific	Cat#12658019
ESF 921 insect cell culture medium	Expression Systems	Cat#96-001-01
ESF 921 Δ, methionine deficient insect cell culture medium	Expression Systems	Cat#96-200

(Continued on next page)

Continued

REAGENT or RESOURCE	SOURCE	IDENTIFIER
HisTrap HP resin	GE Healthcare	Cat#17524802
Glutathione Sepharose 4B resin	GE Healthcare	Cat#17075605
HiTrap Q HP resin	GE Healthcare	Cat#17115401
HiLoad 16/600 Superdex 200 pg resin	GE Healthcare	Cat#28989335
Amylose resin	New England Biolabs	Cat#E8021L
Anti-mouse PVT SPA beads	PerkinElmer	Cat#RPNQ0017
Critical Commercial Assays		
QuickChange II XL Site-Directed Mutagenesis Kit	Agilent Technologies	Cat#200521-5
MEGAscript T7 Transcription Kit	Invitrogen	Cat#AM1334
MEGAclear Transcription Clean-Up Kit	Invitrogen	Cat#AM1908
Xtreme-GENE 9 DNA Transfection Reagent	Roche	Cat#06365787001
TaqMan RNA-to-Ct 1-Step Kit	Life Technologies	Cat#4392653
CellTiter-Glo Luminescent Cell Viability Assay	Promega	Cat#G7570
Deposited Data		
PDB coordinates of the human SF3b ^{core} -PB complex	This work	PDB: 6EN4
PDB coordinates of the protease-resistant core of the human SF3b complex	Cretu et al., 2016	PDB: 5IFE
Cryo-EM model of the yeast B ^{act} complex	Rauhut et al., 2016	PDB: 5LQW
Cryo-EM model of the yeast B ^{act} complex	Yan et al., 2016	PDB: 5GM6
Cryo-EM model of the human B complex	Bertram et al., 2017	PDB: 5O9Z
Cryo-EM model of the yeast B complex	Plaschka et al., 2017	PDB: 5NRL
Experimental Models: Cell Lines		
Hive Five cells (BTI-TN-5B1-4) (<i>Trichoplusia ni</i>)	Thermo Fisher Scientific	Cat#B85502
Sf9 cells (<i>Spodoptera frugiperda</i>)	Thermo Fisher Scientific	Cat#11496015
HeLa S3 cells (isolation of spliceosomes) (<i>Homo sapiens</i>)	Helmoltz Center for Infection Research, Brunswick	N/A
HCT116 cells (<i>Homo sapiens</i>)	ATCC	Cat#CCL-247
HeLa S3 cells (<i>Homo sapiens</i>)	ATCC	Cat#CCL-2.2
Oligonucleotides		
Primer: SF3B1-fwd-del CCGAGGAGTCGACCATGAAGT CTGTCAACG	This work	N/A
Primer: SF3B1-rev-del AGGCTCTAGATTACAGGATGTA GTCCAGTTCGTAGC	This work	N/A
Primer: SF3B1-fwd-R1074H CCCACAAGAAGGCCATCC ATCGCGCTACCGTCAACAC	This work	N/A
Primer: SF3B1-rev-R1074H GTGTTGACGGTAGCGCGA TGGATGGCCTTCTTGTTGG	This work	N/A
Primer: SF3B1-fwd-R1074A CACAAGAAGGCCATCGCG CGCGCTACCGTCAA	This work	N/A
Primer: SF3B1-rev-R1074A TTGACGGTAGCGCGCGC GATGGCCTTCTTGTTG	This work	N/A
Primer: PHF5A-fwd-del GATCTCGAGCCATGGCCAAGC ACCACCCTGA	This work	N/A
Primer: PHF5A-rev-del GCGCTAGCATTACAGGTCGGT CTTAGAAG	This work	N/A
Primer: PHF5A-fwd-Y36A GAAAGTGCGTCATCTGCGA CTCTGCCGTGAGGCCTTG	This work	N/A
Primer: PHF5A-rev-Y36A CAAGGCCTGACGGCAGAGTC GCAGATGACGCACTTTC	This work	N/A

(Continued on next page)

Continued

REAGENT or RESOURCE	SOURCE	IDENTIFIER
Primer: SF3B3-fwd-del TCTCAAAGGCCGAAGTCATCATGAACTA	This work	N/A
Primer: SF3B3-rev-del GTCCACTTCGTCGTTGGTGTAGGAGGCA	This work	N/A
Primer: Ad2-fwd ACTCTCTTCCGCATCGCTGT	This work	N/A
Primer: Ad2-rev CCGACGGGTTTCCGATCCAA	This work	N/A
Primer: Ad2-probe CTGTTGGGCTCGCGGTTG	This work	N/A
Primer: Ftz-fwd TGGCATCAGATTGCAAAGAC	This work	N/A
Primer: Ftz-rev ACGCCGGGTGATGTATCTAT	This work	N/A
Primer: Ftz-probe CGAAACGCACCCGTCAGACG	This work	N/A
Recombinant DNA		
Plasmid: pFL	Dr. Imre Berger, EMBL, Grenoble	N/A
Plasmid: pIDS	Dr. Imre Berger, EMBL, Grenoble	N/A
Plasmid: pFL-10xHIS-TEV	This work, Cretu et al., 2016	N/A
Plasmid: pIDS-GST-PP	This work, Cretu et al., 2016	N/A
Plasmid: pFL-10xHIS-TEV-SF3B3-FLAG/SF3B5/ GST-PP-PHF5A/SF3B1/SF3B6 (<i>H. sapiens</i> full-length codon-optimized synthetic genes, SF3B3 has a TEV protease cleavable N-terminal 10xHIS tag and a C-terminal FLAG tag; PHF5A has an N-terminal PreScission protease (PP) cleavable GST tag)	This work, Cretu et al., 2016	N/A
Plasmid: pFL-10xHIS-TEV-SF3B2-Strep/SF3B4 (<i>H. sapiens</i> full-length codon-optimized synthetic genes, SF3B2 has a TEV protease cleavable N-terminal 10xHIS tag and a C-terminal Strep-tag II)	This work, Cretu et al., 2016	N/A
Plasmid: pFL-10xHIS-TEV-SF3B3-FLAG/SF3B5/GST- PP-PHF5A/SF3B1 (R1074H)/SF3B6 (<i>H. sapiens</i> full-length codon-optimized synthetic genes, SF3B3 has a TEV cleavable N-terminal 10xHIS tag and a C-terminal FLAG tag, PHF5A has an N-terminal PreScission protease (PP) cleavable GST tag, SF3B1 residue R1074 mutated to H)	This work	N/A
Plasmid: pFL-10xHIS-TEV-SF3B3-FLAG/SF3B5/GST- PP-PHF5A (Y36A)/SF3B1 (R1074A)/SF3B6 (<i>H. sapiens</i> full-length codon-optimized synthetic genes, SF3B3 has a TEV cleavable N-terminal 10xHIS tag and a C-terminal FLAG tag, PHF5A has an N-terminal PreScission protease (PP) cleavable GST tag, SF3B1 residue R1074 mutated to A, PHF5A residue Y36 mutated to A)	This work	N/A
Plasmid: pFL-10xHIS-TEV-SF3B3-FLAG/SF3B5/GST- PP-PHF5A (Y36A)/SF3B1/SF3B6 (<i>H. sapiens</i> full-length codon-optimized synthetic genes, SF3B3 has a TEV cleavable N-terminal 10xHIS tag and a C-terminal FLAG tag, PHF5A has an N-terminal PreScission protease (PP) cleavable GST tag, PHF5A residue Y36 mutated to A)	This work	N/A
Plasmid: pFL-10xHIS-TEV-SF3B3 (Δ 1068-1085)-FLAG/ SF3B5/GST-PP-PHF5A (1-98)/SF3B1 (453-1304) (<i>Homo sapiens</i> codon-optimized synthetic genes, SF3B3 has a TEV cleavable N-terminal 10xHIS tag and a C-terminal FLAG tag, PHF5A has an N-terminal PreScission protease (PP) cleavable GST tag, SF3B1 lacks residues 1-452, SF3B3 lacks residues 1068-1085, PHF5A lacks residues 99-110)	This work	N/A

(Continued on next page)

Continued

REAGENT or RESOURCE	SOURCE	IDENTIFIER
Plasmid: pMBP-MS2	Josep Vilardell lab	Addgene Cat#65104
Plasmid: pT7-MINX-M3	Bertram et al., 2017	N/A
Plasmid: pcDNA3.1(+)	Thermo Fisher Scientific	Cat#V79020
Plasmid: pSP65-Ftz	Luo and Reed, 1999	Addgene Cat#11243
Plasmid: pcDNA3.1(+)-Ad2 (wild-type)	This work, Pellizzoni et al., 1998	N/A
Plasmid: pcDNA3.1(+)-Ad2.1 (“enhanced” BS)	This work	N/A
Plasmid: pcDNA3.1(+)-Ad2.11 (“weak” BS, “strong” PPT)	This work	N/A
Plasmid: pcDNA3.1(+)-Ad2.12 (“strong” BS, “weak” PPT)	This work	N/A
Plasmid: pcDNA3.1(+)-Ad2.15 (“weak” BS, “weak” PPT)	This work	N/A
Plasmid: pcDNA3.1(+)-Ad2.2 (“decoy” BS, “strong” PPT)	This work	N/A
Software and Algorithms		
CCP4	Winn et al., 2011	http://www.ccp4.ac.uk/
PHENIX suite	Adams et al., 2010	https://www.phenix-online.org/
XDS	Kabsch, 2010	http://xds.mpimf-heidelberg.mpg.de/
PyMOL	Schrödinger LCC	https://pymol.org/2/
UCSF Chimera	Pettersen et al., 2004	https://www.cgl.ucsf.edu/chimera/
Coot	Emsley et al., 2010	https://www2.mrc-lmb.cam.ac.uk/personal/pemsley/coot/
Grade Web Server	Global Phasing Limited	http://grade.globalphasing.org/cgi-bin/grade/server.cgi/
Arpeggio Web Server	Jubb et al., 2017	http://biosig.unimelb.edu.au/arpeggioweb/
PLIP Web Server	Salentin et al., 2015	https://projects.biotec.tu-dresden.de/plip-web/plip/
ALBULA	Dectris Ltd.	https://www.dectris.com/products/albula-software/
Prism v.6.0	GraphPad Software	https://www.graphpad.com/scientific-software/prism/

CONTACT FOR REAGENT AND RESOURCE SHARING

Requests for resources and reagents should be directed to and will be fulfilled by the Lead Contact, Vladimir Pena (vlad.pena@mpibpc.mpg.de). Requests for cell lines and RNA substrates should be addressed to Silvia Buonamici (silvia_buonamici@h3biomedicine.com) and MTA will be required.

EXPERIMENTAL MODEL AND SUBJECT DETAILS**Cell lines**

HCT116 and HeLa S3 cell lines were obtained from the American Type Culture Collection (ATCC). These cell lines were authenticated using ATCC and tested for mycoplasma contamination tested at IDEXX using IMPACT1 testing. HeLa S3 cells used for isolation of human spliceosomes were obtained from Helmholtz Center for Infection Research (Brunswick) and tested negative for mycoplasma contamination. HeLa S3 cells used for the isolation of spliceosomes were cultured in DMEM/F12 (1:1) medium supplemented with 5% NCS serum at a density of 6.5×10^6 cells/ml. Sf9 (*Spodoptera frugiperda*) and Hive Five (*Trichoplusia ni*) insect cell lines were purchased from Thermo Fisher Scientific and cultured in suspension in Sf-900 III SFM (Thermo Fisher Scientific) and ESF 921 medium (Expression Systems), respectively, at 27°C and 90 rpm. For cloning and bacmid production, we used the *Escherichia coli* BW23474 and DH10MultiBacY strains (gift from Dr. Imre Berger, EMBL, Grenoble), and the *Escherichia coli* XL-10 Gold strain (Agilent Technologies). MBP-MS2 fusion protein used for MS2 affinity selection of spliceosomes was expressed in the *Escherichia coli* strain Rosetta 2 (DE3) (Merck) in 2YT medium at 37°C.

METHOD DETAILS

Expression and purification of recombinant SF3B complexes

The engineered human SF3B core complex was overexpressed in insect cell lines using optimized synthetic genes (GeneArt, Life Technologies), as previously described (Cretu et al., 2016). Briefly, the SF3B3 subunit was cloned in frame with a Tobacco Etch Virus (TEV) protease cleavable N-terminal 10xHIS tag and with a C-terminal FLAG tag. The internal 1068–1085 residues of SF3B3 were removed by “round-the-horn” PCR mutagenesis (Key Resources Table). PHF5A (1–98) was amplified by PCR and fused to a PreScission protease (PP) cleavable GST tag. SF3B5 (full-length) and SF3B1 (453–1304) were cloned by PCR without addition of affinity tags. All four SF3B subunits were placed on a single acceptor vector by the sequential use of the multiplication and the Cre recombination cassettes, as implemented in the Multibac baculovirus/insect cell expression system (Fitzgerald et al., 2006). High Five insect cells (Thermo Fisher Scientific) overexpressing the human SF3B core complex were harvested 72h after infection with recombinant baculoviruses and lysed by sonication in ice-cold buffer A1 (50 mM HEPES-KOH, pH 7.9, 600 mM KCl, 15% (v/v) glycerol, 5 mM 2-mercaptoethanol (2-ME), 30 mM imidazole, pH 8.0) supplemented with a cocktail of protease inhibitors (Roche). The cleared lysate was loaded on a HisTrap HP column (GE Healthcare) equilibrated with buffer A2 (50 mM HEPES-KOH, pH 7.9, 600 mM KCl, 10% (v/v) glycerol, 5 mM 2-ME, 30 mM imidazole, pH 8.0). The bound proteins were eluted by a linear gradient formed between buffer A2 and buffer B (50 mM HEPES-KOH, pH 7.9, 600 mM KCl, 10% (v/v) glycerol, 5 mM 2-ME, 400 mM imidazole, pH 8.0) and incubated with ~20 mL glutathione resin (Glutathione Sepharose 4B, GE Healthcare) in batch for 2h at 4–8°C. The SF3B core complex was eluted from the resin with buffer C (50 mM HEPES-KOH, pH 7.9, 200 mM KCl, 10% (v/v) glycerol, 2 mM DTT, 30 mM L-glutathione reduced) and both the 10xHIS and the GST affinity tags were removed by overnight cleavage with TEV and PP (GE Healthcare) proteases, respectively. The sample was further purified on a HiTrap Q HP column (GE Healthcare) and eluted from the resin using a linear gradient (0%–30%, 50 mL) formed between buffer D (20 mM HEPES-KOH, pH 7.9, 200 mM KCl, 10% (v/v) glycerol, 2 mM DTT) and buffer E (20 mM HEPES-KOH, pH 7.9, 1 M KCl, 5% (v/v) glycerol, 2 mM DTT). SF3B peak fractions were concentrated using an Amicon Ultra-15 centrifugal filter (Millipore) and further purified by size-exclusion chromatography (HiLoad 16/600 Superdex 200 pg, GE Healthcare) in buffer SB (20 mM HEPES-KOH, pH 7.9, 200 mM KCl, 5% (v/v) glycerol, 2 mM DTT). The SF3B core fractions were subsequently concentrated and used fresh in crystallization screening or snap frozen in liquid nitrogen and stored at –80°C. The engineered SF3B core complex contained SF3B1, SF3B3, PHF5A, and SF3B5 in apparently stoichiometric amounts (Figure S1A) and displayed nanomolar affinity for pladienolide B (PB) as also observed with the full-length recombinant SF3B complex (Figure S1B). For the production of selenomethionine-derivatized SF3B core complex, Hive Five insect cells were grown for 48h in ESF 921Δ methionine deficient medium (Expression Systems) and then infected with recombinant baculoviruses. After 12h, the suspension cultures were supplemented with seleno-L-methionine (Sigma) to 0.1g/L and cultured for an additional 60h. R1074H (SF3B1), R1074A (SF3B1), and the Y36A (PHF5A) mutations in the SF3B1-PHF5A tunnel were introduced using a modified protocol based on the QuickChange II XL Site-Directed Mutagenesis Kit (Agilent Technologies). Full-length heptameric human SF3B complexes (SF3B1-SF3B2-SF3B3-SF3B4-SF3B5-SF3B6-PHF5A), used in radioligand binding assays, were overexpressed and purified as previously described (Cretu et al., 2016). All SF3B preparations were analyzed by mass spectrometry (data not shown).

Crystallization and structure determination of the human SF3B core in complex with PB

The engineered human SF3B core complex (SF3B3 (Δ1068–1085)-SF3B1 (453–1304)-PHF5A (1–98)-SF3B5) was concentrated by ultrafiltration to ~6 mg/ml, complexed with PB (purchased from Santa Cruz Biotechnology), added in a 3-fold molar excess over protein, and subjected to initial crystallization screening. Optimized single trapezoidal plates were grown at 2.5–3 mg/mL at 20°C in 1+1 μl hanging drops using reservoir solutions containing 50 mM HEPES-NaOH, pH 7–7.4, 200 mM KCl, and 38%–39% (v/v) pentaerythritol propoxylate (5/4 PO/OH). The best diffracting SF3B-PB co-crystals appeared after 1 day and reached full size after ~5 days. The SF3B core crystals were harvested directly from the mother liquor at 20°C and flashed cooled in liquid nitrogen. Selenium-derivatized crystals, obtained under similar crystallization conditions, were harvested from the mother liquor at 4°C. Diffraction data were collected at 100K on PILATUS 6M-F (25 Hz) at the X10SA beamline (SLS, PSI Villigen, Switzerland). Diffraction data collected from a single crystal were indexed, integrated and scaled with XDS (Kabsch, 2010), and merged with AIMLESS (Evans and Murshudov, 2013), in CCP4 (Winn et al., 2011). The SF3B-PB co-crystal structure was solved by molecular replacement with Phaser-MR (McCoy, 2007) using the previously reported crystal structure of the protease-resistant SF3B core (PDB: 5IFE) (Cretu et al., 2016) as a search model. Like the protease-resistant core complex (Cretu et al., 2016), the ~254 kDa engineered SF3B^{core}-PB complex crystallized in the $P2_12_12_1$ space group (Table 1).

The initial search model was iteratively rebuilt in Coot (Emsley and Cowtan, 2004), followed by refinement with phenix.refine (Adams et al., 2010). As independent means of validating the residue register of the SF3B core model, we collected SAD (single-wavelength anomalous dispersion) data at the Se K-edge (12.662 keV) from selenium-derivatized crystals (Table 1). Careful inspection of the anomalous difference map revealed strong anomalous peaks for 53 out of 54 modeled methionine side chains, in good agreement with our SF3B^{core}-PB structural model (Figures S1F and S1G). We could not assign a Se marker site for SF3B1-M620, likely because of the relative flexibility of the residue (located in the H4 repeat turn). Inspection of the residual $mF_o - DF_o$ map of the refined SF3B core model revealed a strong positive electron density at the interface between SF3B1 and PHF5A. Importantly, the observed positive density differed significantly from the previously reported density, located close to the site (Cretu et al.,

2016). The PB ligand was manually fit into the $mF_o - DF_c$ difference electron density map in Coot with the macrolide moiety of the splicing modulator facing the SF3B3 side (Figures S1C–S1E). In agreement with previous photo-affinity labeling experiments (Kotake et al., 2007), the SF3B3 CTD domain is located $\sim 17\text{\AA}$ from the macrolide cycle, within the effective distance of the reactive probe. The location of the PB ligand was confirmed using both unbiased $mF_o - DF_c$ and polder omit maps (Liebschner et al., 2017) (Figures S1C–S1E). The Grade Web server (Global Phasing Limited) was used to generate geometric restraints for PB refinement. The final model was refined using individual B factors for protein and ligand atoms to a R_{work} value of $\sim 23\%$ and a R_{free} value of $\sim 26\%$ and exhibited good stereochemistry (Table 1). The higher B factors of the macrolide lactone (C1) are consistent with its likely susceptibility to radiation damage. Moreover, this observation also agrees with the described tendency of pladienolides to undergo hydrolysis of the C1 bond in aqueous media (Villa et al., 2013). The final model comprises the HEAT domain of SF3B1 (residues 463–1304), SF3B3 (residues 1–1217, lacking the 1068–1085 loop region), SF3B5 (residues 15–79) and PHF5A (residues 6–98). The 453–462 N-terminal residues of SF3B1, as well as several internal SF3B3 loop regions (646–661; 692–694; 829–832), could not be traced in the electron density, likely, owing to relative flexibility/disorder. All structural figures were generated with PyMOL (versus 1.8.4.1, Schrödinger LLC). The contact sites between PB and the SF3B core were identified with Arpeggio (Jubb et al., 2017) and PLIP (Salentin et al., 2015), and analyzed in PyMOL. The SF3B1–PHF5A tunnel was computed using a modified HOLLOW script (Abe and Hiraki, 2009) and rendered in PyMOL. Structural alignment of herboxidiene (Edmunds et al., 2000) and PB (Figure 4) was carried out in UCSF Chimera (Pettersen et al., 2004).

Structural superposition of SF3B1 and Hsh155p

Comparison of the SF3B1 HEAT helix in the PB-bound state (open) with the yeast ortholog in the B_{act} spliceosome (closed) shows major conformational differences (rmsd of 5.2\AA , 710 C α) (Figure S4A). Analyses of individual pairs of HEAT repeats (Figure S4E) showed small differences at the interfaces between H2–H3, H7–H8, H11–H12, while major variations are present at the interfaces of H15–H16 (rmsd of 2.06 , 66 C α) and H16–H17 (rmsd of 1.22 , 72 C α). In contrast, the intramolecular interfaces of H15 and H17 with the neighboring repeats remained largely unchanged (H14–H15 – rmsd of 0.67 (71 C α), H17–H18 – rmsd of 0.64 (69 C α). As a result, the $\sim 23^\circ$ rotation of the H15 repeat over the H16 hinge, toward the convex side of SF3B1, would induce a counterclockwise movement of the entire H1–H15 arch. Except for the flexible BPB domain of SF3B3, all other SF3B modules behave as rigid bodies with respect to the H17–H20 repeats and superimpose onto the yeast proteins without major clashes (Figures S4D and S4E).

The large-scale reconfiguration of the SF3B1 superhelix after rotation of the H15–H17 hinge would shorten the distance between the terminal HEAT repeats to a similar extent as observed when comparing the “open” and “closed” conformation (from $\sim 25\text{\AA}$ to $\sim 18\text{\AA}$). However, smaller additional rearrangements at the H2–H3 and H7–H8 interfaces – likely, induced upon interaction with the BS and polypyrimidine regions of the intron and/or with additional splicing factors – might be required to achieve a state that is virtually identical to the “closed” state.

Changes in the configuration of the SF3B1 helix are also coupled with additional rearrangements that occur at the interfaces between SF3B1 and PHF5A and between SF3B1 and the BPA domain of SF3B3. At the second contact site, the C-terminal extension of PHF5A (aa 91–98), undergoes a forward movement with respect to its globular domain. As a result, it interacts with the H2 repeat of SF3B1 replacing previous contacts of the E48, Y51 and Y54 residues (E48–H550; E48–K554; Y51–Q547; Y54–Q547); these residues are now involved in contacts with the H5–H6 repeats (E48–C677, Y51–E714). Because in isolation the C terminus of PHF5A (Rds3p in yeast) is disordered, this region likely folds to an α helix, as seen in the yeast spliceosome, upon simultaneous binding to SF3B1 and to the minor groove of the U2/BS helix. Consistent with a rotation around the H16 hinge, the interfaces between the BPA domain of SF3B3 and PHF5A are not significantly changed.

Cell viability assays

For CellTiter-Glo analysis, 500 cells (HCT116 parental, HCT116 Y36C and HCT116 R1074H generated as described in Teng et al., 2017) were seeded in each well of a 384-well plate the day before compound addition. An 11 pt serial dilution was used starting with a top final dosage of 10 mM for 10 additional doses. DMSO percentage was maintained throughout and a DMSO-only control was included. Seventy-two hours post compound addition, CellTiter-Glo reagent was added to the medium, incubated and assayed on EnVision Multilabel Reader (PerkinElmer). The luminescence value from each treatment sample was normalized to the average value of the respective DMSO control. The dosage response curve plots were generated using Prism 6 (GraphPad) and fit using nonlinear regression analysis and the log (inhibitor) versus response-variable slope (four parameters).

HeLa nuclear extract preparation

HeLa S3 cell pellets were resuspended in hypotonic buffer (10 mM HEPES pH 7.9, 1.5 mM MgCl_2 , 10 mM KCl, 0.2 mM PMSF, and 0.5 mM DTT) and the suspension was brought up to a total of 5 packed cell volume (PCV). After centrifugation, the supernatant was discarded, and the cells were brought up to 3 PCV with hypotonic buffer and incubated on ice for 10 minutes. Cells were lysed using a Dounce homogenizer and then centrifuged. The supernatant was discarded, and the pellet was resuspended with $\frac{1}{2}$ packed nuclear volume (PNV) of low salt buffer (20 mM HEPES pH 7.9, 1.5 mM MgCl_2 , 20 mM KCl, 0.2 mM EDTA, 25% glycerol, 0.2 mM PMSF, 0.5 mM DTT), followed by $\frac{1}{2}$ PNV of high salt buffer (same as low salt buffer except 1.4M KCl was used). The nuclei were gently mixed

for 30 minutes before centrifuging. The supernatant (nuclear extract) was then dialyzed into storage buffer (20 mM HEPES pH 7.9, 100 mM KCl, 0.2 mM EDTA, 20% glycerol, 0.2 mM PMSF, 0.5 mM DTT). Protein concentration was determined using NanoDrop 8000 UV-Vis spectrophotometer (Thermo Fisher Scientific).

In vitro splicing assays

All Ad2-derived (Pellizzoni et al., 1998) sequences were cloned into the pcDNA3.1(+) vector (Promega) using 5' EcoRI and 3' XbaI restriction sites. The plasmids were linearized using XbaI and used as DNA templates in the *in vitro* transcription reactions. The FtzΔi intron-less plasmid (Luo and Reed, 1999) was linearized using EcoRI. All RNAs were *in vitro* transcribed and then purified using MEGAscript T7 (Invitrogen) and MEGAclear (Invitrogen) kits, respectively. For splicing reactions using Ad2 variant pre-mRNAs, 1 μL reactions were prepared using 8 μg nuclear extracts prepared from HeLa S3, 2 ng pre-mRNA, 0.2 ng FTZΔi, and varying concentrations of PB, PB-OH or DMSO. After a 15-minute pre-incubation at 30°C, 1 μL splicing activation buffer (0.5 mM ATP, 20 mM creatine phosphate, 1.6 mM MgCl₂) was added, and the reactions were incubated for 90 minutes at 30°C. The reactions were then quenched with 13 μL DMSO, and 25 nL was used for RT-qPCR. RT-qPCR reactions were prepared using TaqMan RNA-to-C_T 1-step kit (Life Technologies), RNA from splicing reactions, Ad2 (forward: ACTCTCTCCGCATCGCTGT; reverse: CCGACGGGTTCC GATCCAA; probe: CTGTTGGGCTCGCGGTTG) and Ftz (forward: TGGCATCAGATTGCAAAGAC; reverse: ACGCCGGGTGATG TATCTAT; probe: CGAAACGCACCCGTCAGACG) mRNA primer-probe sets. Prism 6 (GraphPad) was used for non-linear regression curve fitting of the formed spliced product and normalized to the control (DMSO) sample.

Scintillation proximity assays/competitive binding assay

Batch immobilization of anti-FLAG antibody (Sigma-Aldrich) to anti-mouse PVT SPA scintillation beads (PerkinElmer) was prepared as follows. For every 1.5mg of beads, 10μg antibody was prepared in 150μl PBS. The antibody-bead mixture was incubated for 30min at RT and centrifuged at 18,000g for 5min. 150μl PBS was used to resuspend every 1.5mg antibody-bead mixture. The purified SF3B full-length complexes were tested for [³H]-labeled pladienolide probe binding ([³H]-PB), synthesized as previously described (Kotake et al., 2007). 100μl binding reactions were prepared with 50μl bead slurry and 0 or 10nM protein in buffer (20mM HEPES pH 8, 200mM KCl, 5% glycerol). The mixture was incubated for 30min, and 1 nM or 10 nM [³H]-probe was added. The mixture was incubated for 30min, and luminescence signals were read using a MicroBeta2 Plate Counter (PerkinElmer). Compound competition studies were performed with the full-length heptameric SF3B and the SF3B core complex immobilized using anti-SF3B3 antibody. 100μl binding reactions were prepared with 50μl bead slurry, 12.5nM protein in buffer and compounds PB and PB-OH at varying concentrations. After a 30-min pre-incubation, 1 nM [³H]-PB was added. The reactions were incubated for 30min, and luminescence signals were read. SF3B complexes from HeLa nuclear extracts were immunoprecipitated using anti-SF3B1 antibody. Batch immobilization of anti-SF3B1 antibody (MBL) to anti-mouse PVT SPA scintillation beads (PerkinElmer) was prepared as follows: for every 2.5mg of nuclear extracts, 5μg anti-SF3B1 antibody and 1.5mg of beads were mixed in 150μl PBS. The antibody-bead mixture was incubated for 30min at RT and centrifuged at 18,000g for 5min. The beads were suspended and added to the prepared nuclear extracts. The slurry was incubated for 2h at 4°C with gentle mixing. The beads were then collected by centrifuging at 18,000g for 5min and washed twice with PBS+0.1% Triton X-100. After a final centrifugation step, every 1.5mg of beads was suspended with 150μl of PBS. 100 μL binding reactions were prepared by adding varying concentrations of PB or PB-OH, and after 30min pre-incubation, 2.5nM [³H]-probe was added. The mixture was incubated for 30min, and luminescence signals were read. Prism 6 (GraphPad) was used for non-linear regression curve fitting of the data.

Affinity purification of B complexes and splicing chase experiments

In vitro assembled spliceosomal B complexes were purified by gradient centrifugation, followed by MS2 affinity-selection using amylose beads (New England Biolabs) as previously described (Bessonov et al., 2008). Briefly, ³²P-labeled MINX containing MS2 aptamers at its 3' was incubated with a 20-fold molar excess of MS2-MBP protein. Standard splicing reactions containing 10 nM pre-mRNA were incubated at 30°C for 6 min and chilled on ice. Splicing complexes were subsequently separated on a linear 10%–30% (v/v) glycerol gradient containing G-150 buffer (20 mM HEPES-KOH, pH 7.9, 150 mM KCl, 1.5 mM MgCl₂) by centrifugation for 16 h at 23000 rpm in a Sorvall Surespin 630 rotor. Complexes in the 45S peak fractions were loaded onto amylose beads (NEB), and after washing with G-75 buffer (G buffer with 75 mM KCl), bound spliceosomal complexes were eluted with 20 mM maltose in G-75 buffer. RNA was recovered from the purified complexes, separated on a denaturing polyacrylamide gel and visualized by silver staining (Figure S5A). For *in vitro* chase experiments, HeLa nuclear extract was treated with micrococcal nuclease (MN) as described previously (Makarov et al., 2002). Affinity-purified B complexes formed on ³²P-labeled MINX-MS2 pre-mRNA were incubated with splicing buffer alone (60 mM KCl, 3 mM MgCl₂, 2 mM ATP, 20 mM creatine phosphate, 20 mM HEPES-KOH, pH 7.9), or in the presence of 20% (v/v) MN-treated HeLa nuclear extract containing 0 or 6 μM PB or purified B complexes were pre-incubated with 1.5 or 6 μM PB for 30 min on ice prior to addition of MN-treated nuclear extract. A 10-fold molar excess of unlabelled MINX-MS2 pre-mRNA was added to prevent the reassembly of snRNPs (that potentially dissociate from the purified complexes) on the radiolabeled pre-mRNA. The reaction was incubated at 30°C for 0, 30 or 60 min. RNA was recovered, separated on a 14% denaturing polyacrylamide gel, and visualized with a Typhoon phosphorimager (GE Healthcare) (Figure S6B). The % mRNA formed was quantified using ImageQuantTL (GE Healthcare) and calculated by dividing the amount of mRNA by the amount of pre-mRNA, lariat-intermediate and splicing products (Figure S5B).

QUANTIFICATION AND STATISTICAL ANALYSIS

All statistical analyses were carried out with Prism 6 (GraphPad). For the biochemical (binding and *in vitro* splicing assay) and viability assays each concentration was tested in triplicate and each experiment was repeated multiple times (2 times for the biochemical assays and 3 times for the viability assay). The compound concentrations used for the assay window was estimated such that the IC_{50} was near the center of the fitted curve. All the experiments were repeated multiple times (2 times for the biochemical assays and 3 times for the viability assays). No data were excluded from the analysis. No randomization was required. Clear description of statistics (central tendency, variation, exact sample size) is included in figure legends.

DATA AND SOFTWARE AVAILABILITY

The accession number for the coordinates reported in this paper is PDB: 6EN4.

Molecular Cell, Volume 70

Supplemental Information

Structural Basis of Splicing Modulation

by Antitumor Macrolide Compounds

Constantin Cretu, Anant A. Agrawal, Andrew Cook, Cindy L. Will, Peter Fekkes, Peter G. Smith, Reinhard Lührmann, Nicholas Larsen, Silvia Buonamici, and Vladimir Pena

Supplemental Information

Supplemental Figures

Figure S1

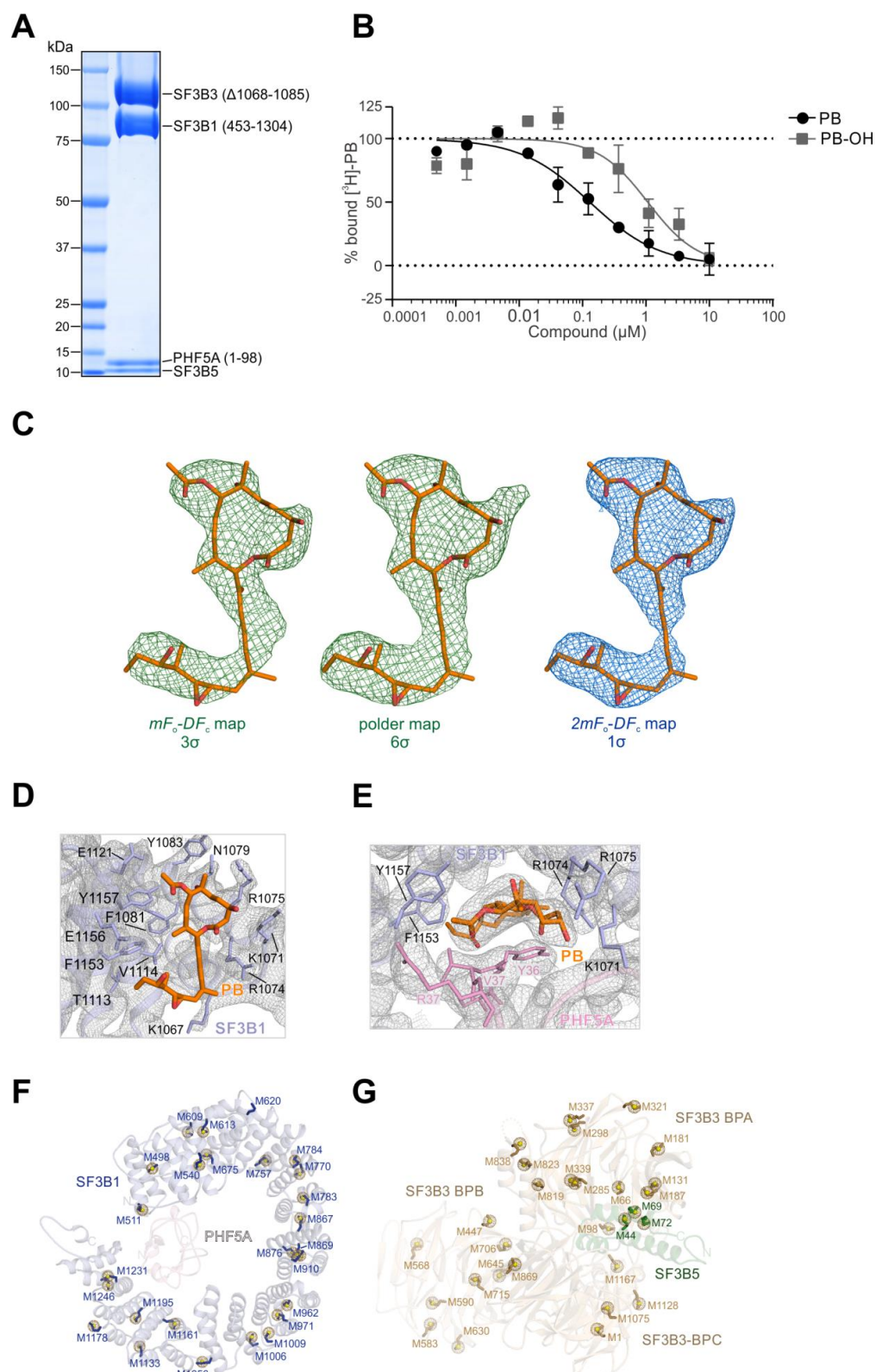


Figure S2

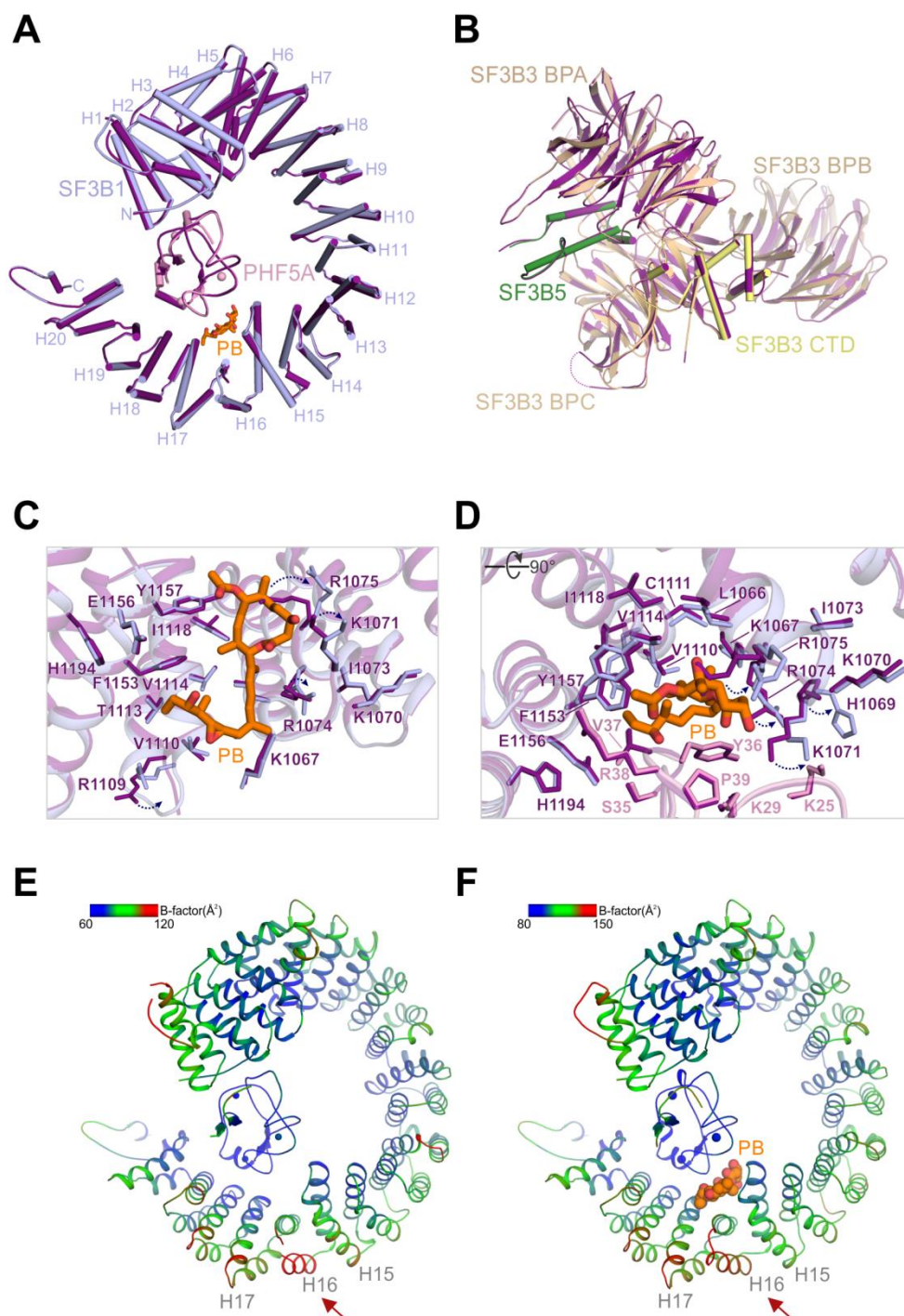
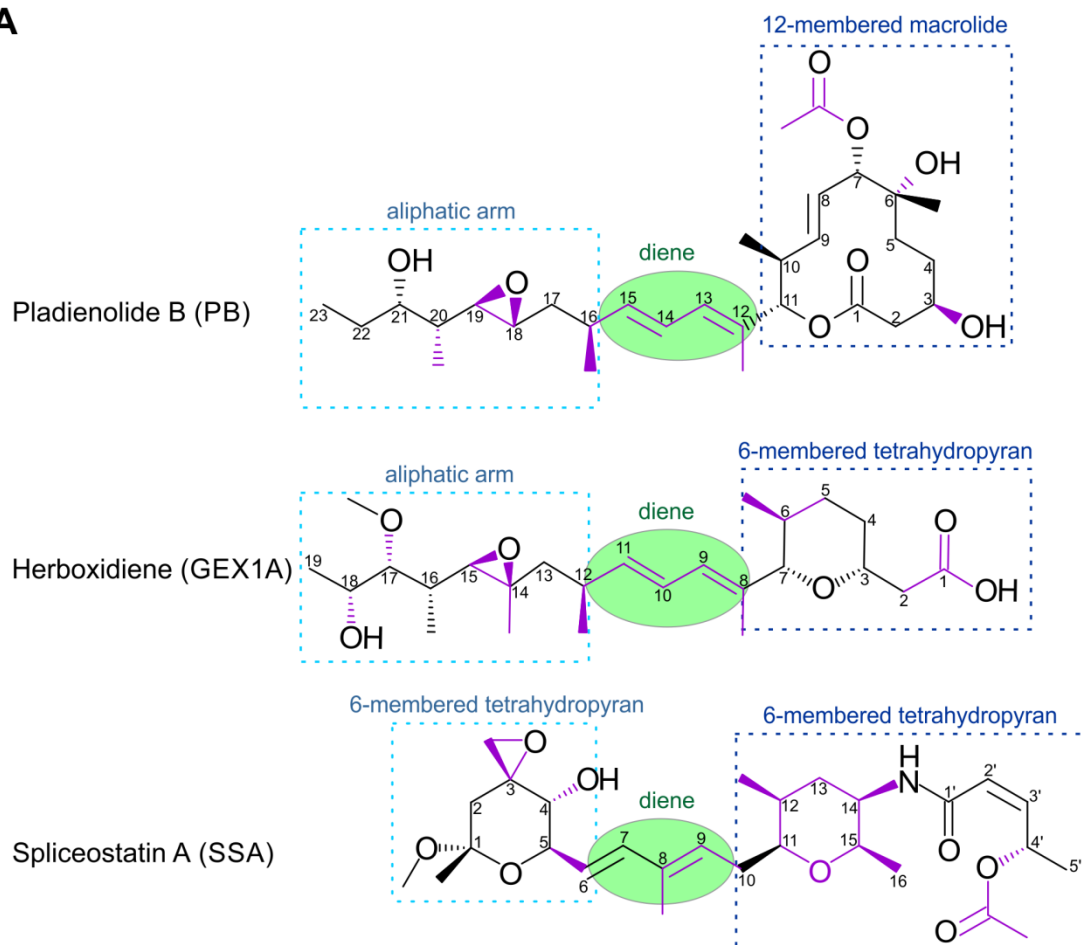


Figure S3

A



B

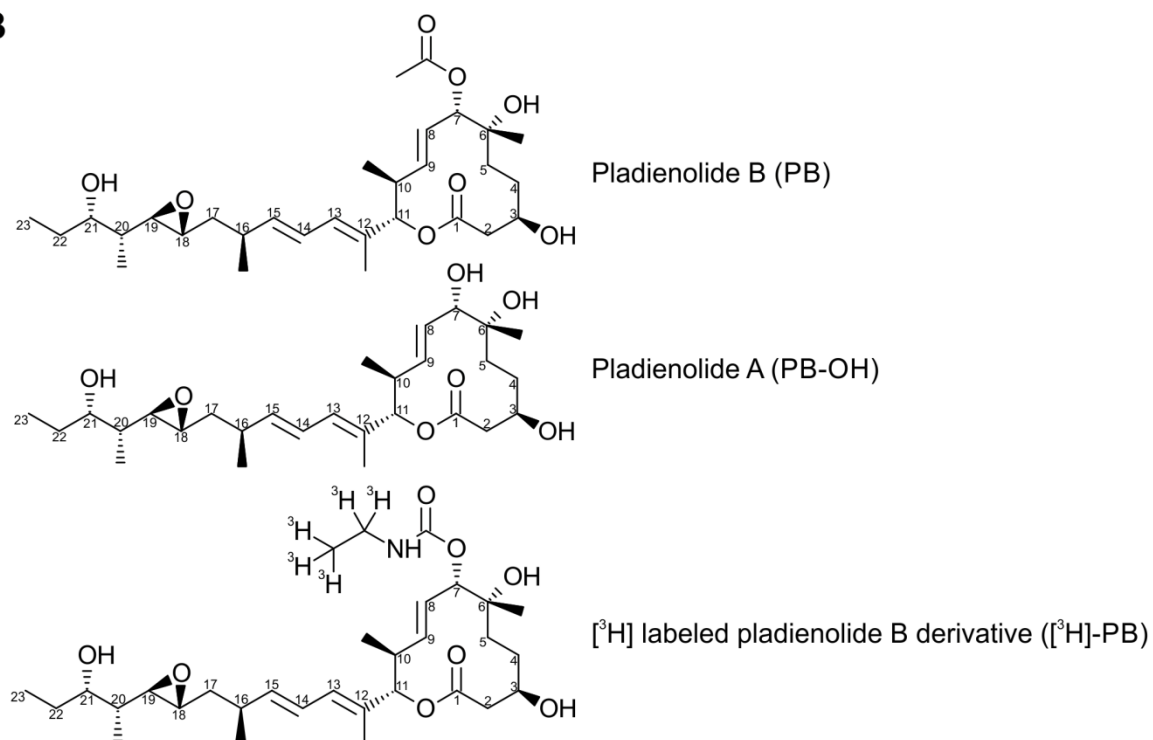


Figure S4

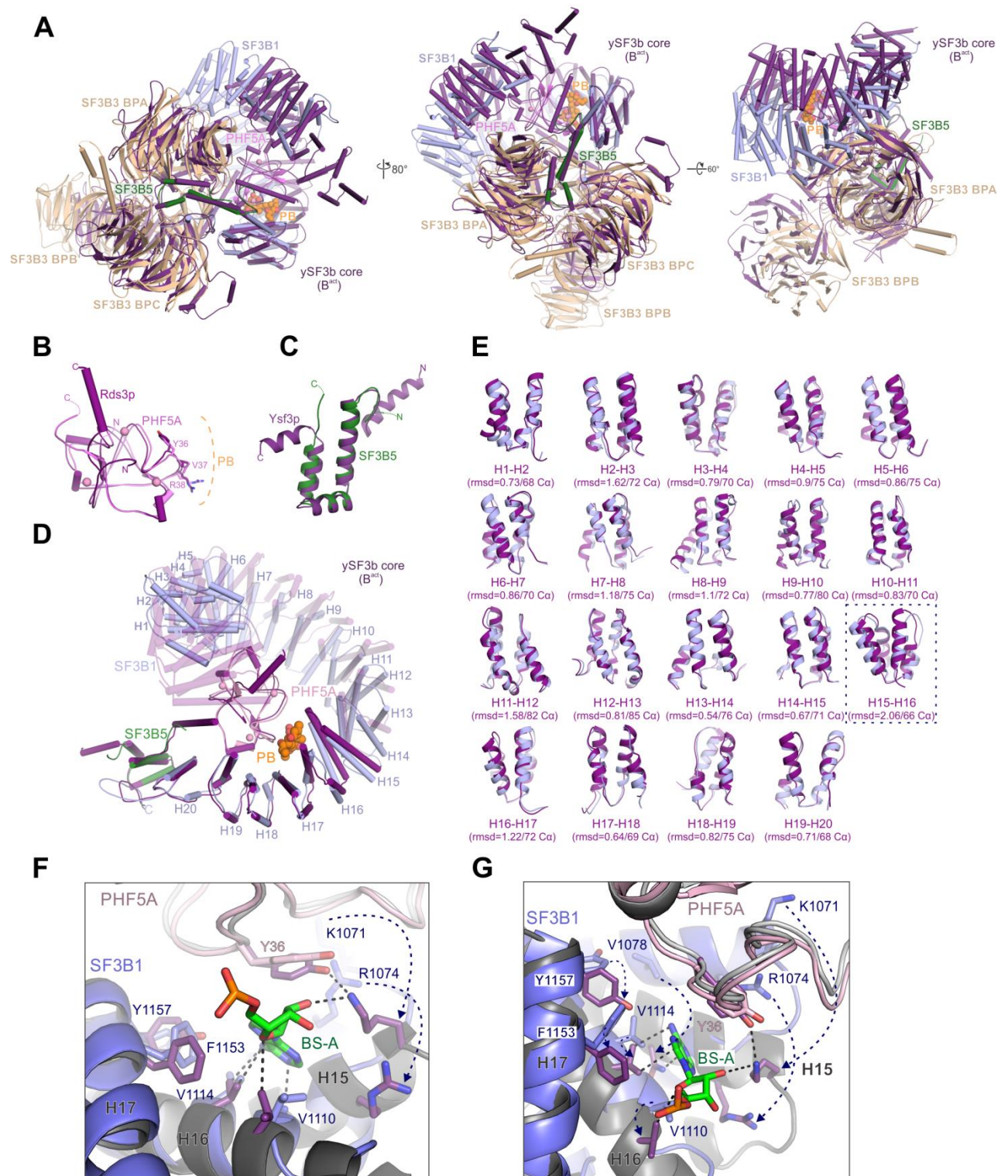


Figure S5

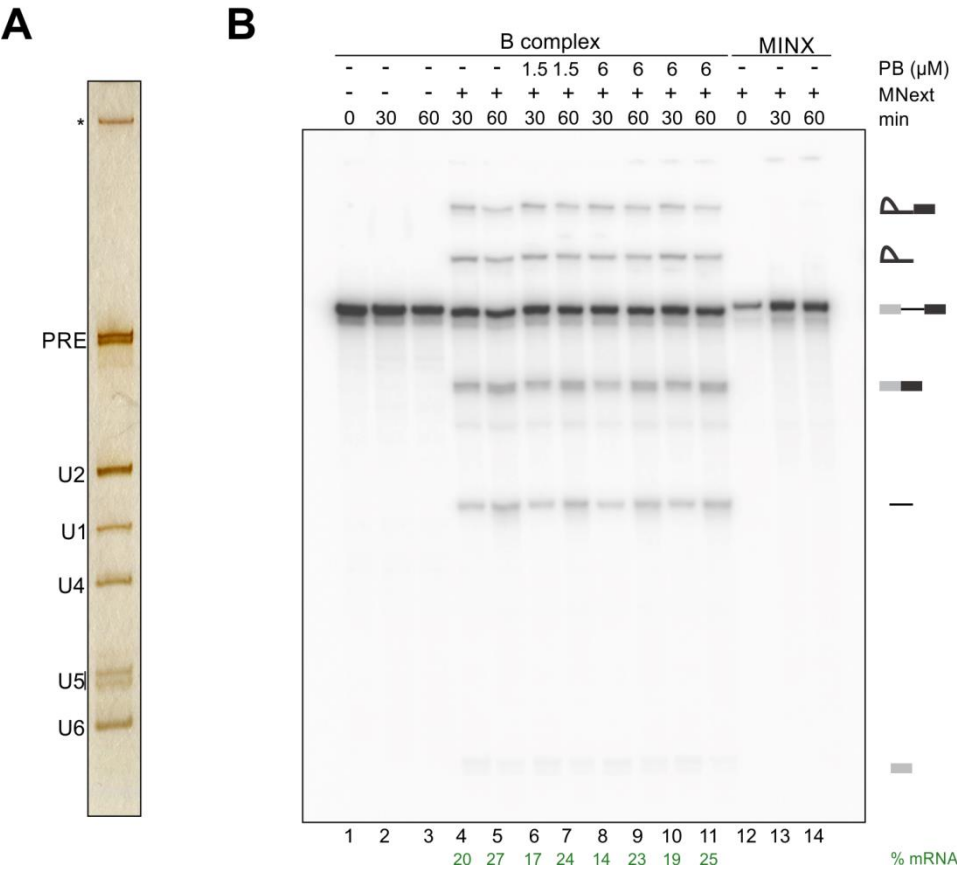


Figure S6

A

Ad2-derived splicing substrates	Sequence (3' splice site)	PB IC ₅₀ (nM)	PB-OH IC ₅₀ (nM)	Fold change
Enhanced BS (Ad2.1)	<div><div>-32</div><div>-14</div><div>-1</div></div> <div>TCAT<u>ACTTAA</u>TCCTGTCCC<u>TTTTTTT</u>CCACAG</div>	19	-	>100
Wild-type (Ad2)	<div><div>-32</div><div>-14</div><div>-1</div></div> <div>TCAT<u>ACTTAA</u>TCCTGTCCC<u>TTTTTTT</u>CCACAG</div>	18	1589	88.3
Strong BS/weak PPT (Ad2.12)	<div><div>-32</div><div>-14</div><div>-1</div></div> <div>TCAT<u>ACTTAA</u>TCCTGTCCC<u>CCCCCCCC</u>CCACAG</div>	19	1235	65
Weak BS/strong PPT (Ad2.11)	<div><div>-32</div><div>-14</div><div>-1</div></div> <div>TCAT<u>AGTTAA</u>TCCTGTCCC<u>TTTTTTT</u>CCACAG</div>	22	224	10.2
Weak BS/weak PPT (Ad2.15)	<div><div>-32</div><div>-14</div><div>-1</div></div> <div>TCAT<u>AGTTAA</u>TCCTGTCCC<u>CCCCCCCC</u>CCACAG</div>	18	158	8.8
Decoy BS/strong PPT (Ad2.2)	<div><div>-32</div><div>-14</div><div>-1</div></div> <div><u>TACTACTTAA</u>TCCTGTCCC<u>TTTTTTT</u>CCACAG</div>	29	54	1.9

B

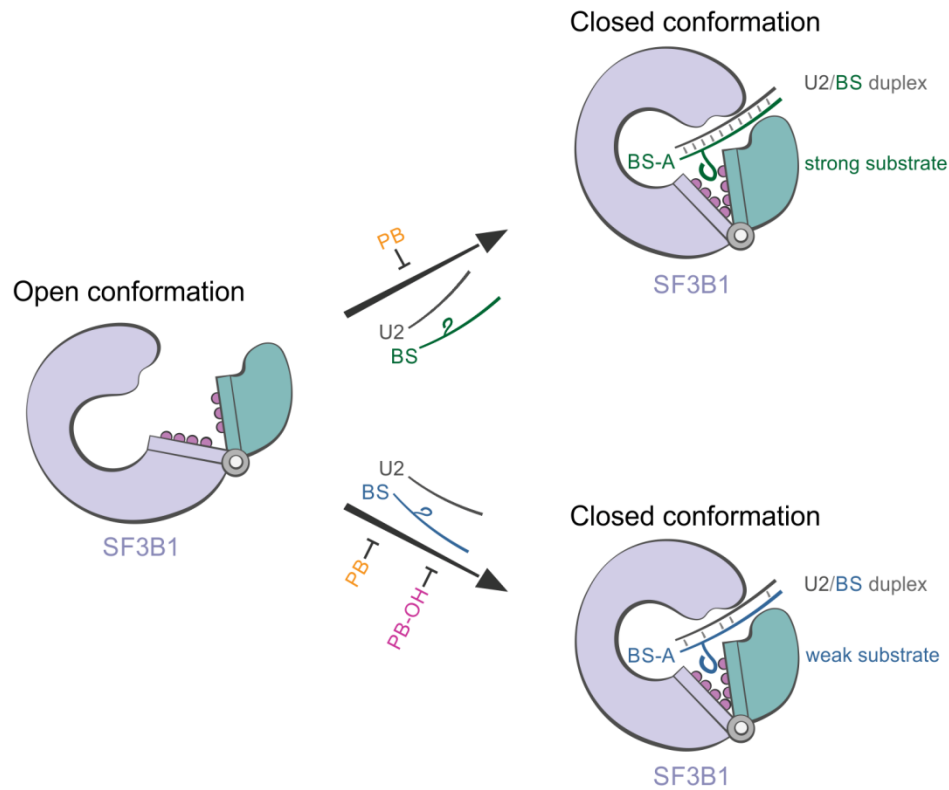


Figure S1. Crystal structure of an engineered human SF3B core in complex with pladienolide B (PB). Related to Figure 1.

(A) Coomassie-stained SDS-PAGE analysis of an engineered human SF3B core complex, reconstituted by co-expression in insect cells, after size-exclusion chromatography. SF3B3 (lacking residues 1068-1085), SF3B1 (residues 453-1304), PHF5A (residues 1-98), and SF3B5 (full-length) appear to be present in stoichiometric amounts. (B) Scintillation proximity assays of the human SF3B core in the presence of a tritiated PB derivative ($[^3\text{H}]$ -PB) and unlabelled PB or PB-OH as competitors. The engineered SF3B core binds $[^3\text{H}]$ -PB suggesting that the minimal complex contains an intact PB binding site ($\text{IC}_{50} = 130 \text{ nM}$ for PB and $\text{IC}_{50} = 1070 \text{ nM}$ for PB-OH). (C) Electron density maps of the PB ligand calculated from the refined structure. Residual $mF_o - DF_c$ (contoured at 3σ) and polder (contoured at 6σ) omit maps are displayed next to a $2mF_o - DF_c$ map (contoured at 1σ). The PB ligand is depicted as orange sticks. (D) Electron density map of SF3B1 at the PB binding site. The $2mF_o - DF_c$ map (grey mesh, 1σ) is displayed around SF3B1 (light blue) and the PB ligand is shown as orange sticks (see also Figure 1B). (E), Electron density map of the SF3B1-PHF5A PB binding tunnel. The $2mF_o - DF_c$ map (grey mesh, 1σ) is shown around SF3B1 (light blue), PHF5A (pink), and PB (orange). Key residues lining the SF3B1-PHF5A tunnel are depicted as sticks. (F), (G) Selenium marker sites validate the residue register of the SF3B core structure. Selenium sites were identified using SAD log-likelihood gradient maps and are shown as yellow spheres. The modeled methionine side chains are shown as sticks. SF3B1, SF3B3, SF3B5, and PHF5A are colored as in Figure 1.

Figure S2. Structural rearrangements of the SF3B core complex in the presence of pladienolide B (PB). Related to Figure 2.

(A) Superposition of the SF3B1 and PHF5A SF3B subunits in the presence and absence of the PB ligand. SF3B1 and PHF5A from the PB co-crystal structure are coloured light blue and pink, respectively, while the subunits from the apo SF3B core structure (PDB 5IFE) are coloured dark purple. The individual HEAT repeats of SF3B1 are labelled H1-H20. PB is depicted as sticks and is coloured orange. PHF5A's Zn atoms are indicated as spheres. (B) Superposition of the SF3B3-SF3B5 module of the SF3B core in the presence and absence of PB. SF3B3 and SF3B5 subunits are coloured as in Figure 1, while the SF3B3-SF3B5 module from the apo structure (PDB 5IFE) is in dark purple. The engineered SF3B3 has a shorter insertion loop in the 6th blade of the BPC β -propeller domain as a result of the removal of residues 1068-1085. (C), (D) Comparison of SF3B1 and PHF5A crystal structures at the PB binding site. The SF3B1 HEAT domain and PHF5A from the apo SF3B core structure (PDB 5IFE) are depicted as cartoons and are coloured in dark purple. The PB ligand is represented as orange sticks. SF3B1 and PHF5A subunits from the PB co-crystal structure are coloured light blue and pink, respectively. Key SF3B1 and PHF5A residues lining the PB binding tunnel are shown as sticks. SF3B1-K1071, SF3B1-R1074, and SF3B1-R1075 residues from the SF3B1-PHF5A tunnel are rearranged to accommodate the ligand (arrows), while PHF5A-Y36A and PHF5A-R38 residues adopt similar positions in both crystal structures. (E) Cartoon representation of SF3B1 and PHF5A subunits from the apo SF3B core crystal structure (PDB 5IFE) coloured according to the local B-factors (blue-green-red). Note that HEAT repeat H16 shows higher B factors compared to the neighbouring HEAT repeats of SF3B1. (F) Cartoon representation of SF3B1 and PHF5A subunits from the SF3B-PB co-crystal structure coloured according to their local B-factors (blue-green-red). The PB ligand (orange spheres)

binds SF3B1 in the proximity of the H16 repeat, apparently stabilizing this more dynamic region of SF3B1.

Figure S3. Chemical structures of SF3B modulators. Related to Figures 3 and 4.

(A) Representative compounds belonging to the pladienolide (PB), herboxidiene (GEX1A), and spliceostatin (SSA) families of splicing modulators are shown. All compounds share a common diene group (light green) which connects two larger moieties, specific for each family of modulators. Herboxidienes have in common with pladienolides a similar aliphatic arm and with spliceostatins a 6-membered functionalized pyran ring. Chemical groups required for the activity of the compounds are highlighted in purple. (B) Structures of PB derivatives used in this study.

Figure S4. Structural comparison of the human SF3B-PB co-crystal structure with the yeast SF3B core. Related to Figure 5.

(A) Three different views of the human SF3B-PB structure superimposed onto the yeast SF3B core in the activated spliceosome. Human SF3B subunits are coloured and displayed as in Figure 1A. The yeast SF3B core (containing the Hsh155p HEAT domain, Rse1p, Rds3p, Ysf3p) is coloured dark purple. PB is depicted as orange spheres. Note that SF3B3, with the exception of its flexible BPB domain, SF3B1 H16-H20, PHF5A, and SF3B5 superimpose onto the yeast proteins without major clashes. The H1-H15 arch of SF3B1 behaves largely as a rigid body with respect to the SF3B1 (H16-H20)-PHF5A-SF3B3 (BPA-BPC)-SF3B5 module and is arranged differently in the two structures. (B) Superposition of PHF5A onto Rds3p as part of the SF3B1 (H16-H20)-PHF5A-SF3B3 (BPA-BPC)-SF3B5 module. Note that PHF5A residues located at the PB binding tunnel (Y36, V37, R38) face the same side, but adopt different conformations in the two structures. (C) Superposition of SF3B5 onto Ysf3p as part of the SF3B1 (H16-H20)-PHF5A-SF3B3 (BPA-BPC)-SF3B5 module. (D) Superposition of SF3B1 (H16-H20), SF3B5, and PHF5A onto the yeast SF3B core (dark purple) as part of the SF3B1 (H16-H20)-PHF5A-SF3B3 (BPA-BPC)-SF3B5 module. Note that the major difference between the two structures results from the different arrangement of the SF3B1 H1-H15 arch with respect to the SF3B1 (H16-H20)-PHF5A-SF3B3 (BPA-BPC)-SF3B5 module. SF3B3 is not shown. (E) Comparison of SF3B1's intramolecular interfaces between consecutive pairs of HEAT repeats in the SF3B-PB and yeast SF3B core structures. The largest difference between the two structures was detected at the H15-H16 interface (r.m.s.d. = 2.06, 66 C α). Corroborated by the higher B-factor values (Figure S2F), this reveals the location of the hinge region. (F), (G) Structural superpositions of the H15-H17 hinge regions of SF3B1 (blue) and Hsh155p (dark grey), shown in two different orientations (left and right). PB is omitted for clarity sake and the BS-A is shown as sticks (green). PHF5A and the *S. cerevisiae* orthologue are coloured pink and light grey, respectively. SF3B1 residues that belong to the PB-binding site and the equivalent residues from Hsh155p are depicted in blue and dark purple, respectively.

Figure S5. Addition of PB to purified spliceosomal B complexes has no substantial effect on their ability to catalyse pre-mRNA splicing in the presence of MN-treated extract. Related to Figure 5.

(A) RNA composition of the affinity-purified B complexes. RNA was analyzed by denaturing PAGE and visualized by staining with silver. B complexes formed on ³²P-labelled MINX-MS2 pre-mRNA were affinity purified as described in the Online Methods. Asterisk, RNA in the loading well of the gel. The presence of the U1, U2, U4, U5, and U6 snRNAs confirms that spliceosomal B complexes were isolated. (B) Purified B complexes were incubated at 30°C for the indicated times (0, 30, 60 min) under splicing conditions in the presence of buffer alone (lanes 1-3) or micrococcal nuclease-treated HeLa nuclear extract (MNext) (lanes 4-14). PB (1.5 or 6 μM) was added directly to the purified B complexes, followed by a 30 min incubation on ice, prior to performing the chase with MN-treated extract (lanes 6-9) or PB (6 μM) was added to the MN-treated extract (lanes 10-11). As a control for complete MN-digestion, no splicing was observed when ³²P-labelled MINX-MS2 pre-mRNA was incubated with MNext (lanes 12-14). RNA was analysed by denaturing PAGE and visualized with a Phosphorimager. The positions of the pre-mRNA, splicing intermediates and products are indicated on the right. The % mRNA formed (quantitated with a Phosphorimager) is indicated below selected lanes. Addition of PB had no substantial effect on the ability of B complexes to catalyse splicing after chasing with MNext. This is consistent with the idea that once SF3B has adopted a closed conformation, as observed in the B complex, PB no longer can bind and inhibit splicing.

Figure S6. Splicing modulators may act as competitive BS antagonists. Related to Figure 6.

(A) Summary of the substrates and *in vitro* splicing assays carried out in the presence of PB or PB-OH. The IC₅₀ values were obtained from non-linear regression curve fitting.

(B) The discriminatory action of splicing modulators towards various 3'SS sequences is a consequence of the competition between substrates and modulators for the “open” conformation of SF3B1 (see also Figure 5E). Potent modulators, such as PB, exhibit high affinity for the “open” conformation of SF3B1, inhibiting the transition to the “closed” conformation even for “strong” substrates. Conversely, modulators that display lower affinities for the “open” state of SF3B1, such as PB-OH, can inhibit efficiently only “weak” substrates. PB is colored in orange, while PB-OH is colored in pink. All the other elements are depicted and labeled as in the Figure 5E.